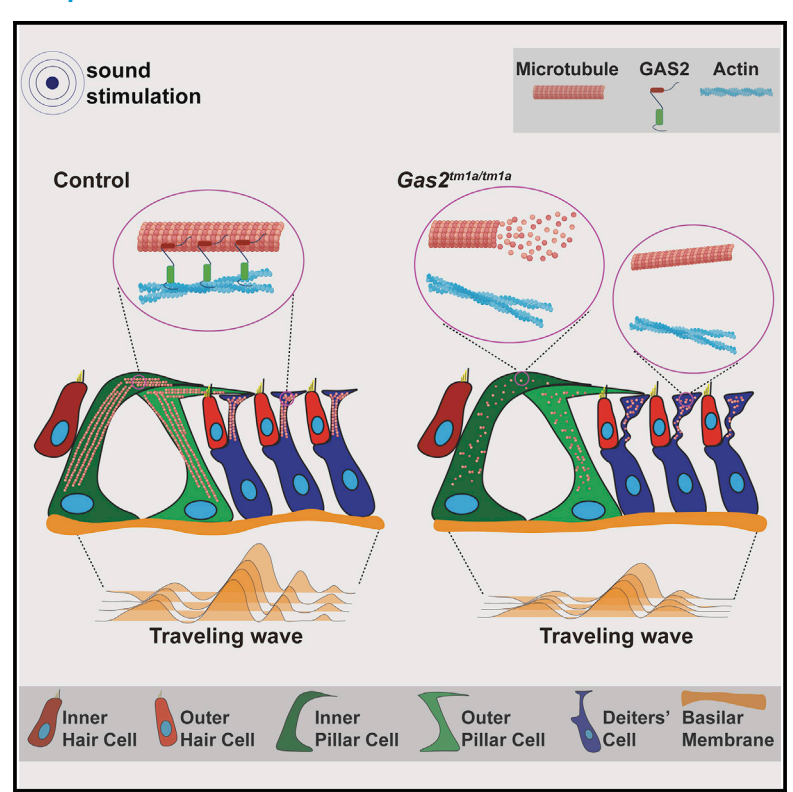
Cochlear supporting cells require GAS2 for cytoskeletal architecture and hearing

Graphical abstract



Authors

Tingfang Chen, Alex M. Rohacek, Matthew Caporizzo, ..., Hannie Kremer, Benjamin L. Prosser, Douglas J. Epstein

Correspondence

epsteind@pennmedicine.upenn.edu

In brief

Chen et al. describe how mutations in GAS2, encoding a microtubule-associated protein, cause hearing loss in mice and humans. They show that microtubule bundle integrity is compromised in cochlear supporting cells from Gas2 mutants, causing defects in the amplification and propagation of sound waves in the cochlea.

Highlights

- GAS2 mutations cause hearing loss in mice and humans
- GAS2 maintains microtubule bundle integrity in cochlear supporting cells
- Supporting cell defects in Gas2 mutants compromise cochlear mechanics





Article

Cochlear supporting cells require GAS2 for cytoskeletal architecture and hearing

Tingfang Chen, 1,8 Alex M. Rohacek, 1,8 Matthew Caporizzo, 2 Amir Nankali, 3 Jeroen J. Smits, 4 Jaap Oostrik, 4 Cornelis P. Lanting, 4 Erdi Kücük, 5 Christian Gilissen, 5 Jiddeke M. van de Kamp, 6 Ronald J.E. Pennings, 4 Staci M. Rakowiecki, Klaus H. Kaestner, Kevin K. Ohlemiller, John S. Oghalai, Hannie Kremer, Benjamin L. Prosser, and Douglas J. Epstein^{1,9,*}

- ¹Department of Genetics, Perelman School of Medicine, University of Pennsylvania, Philadelphia, PA, USA
- ²Department of Physiology, Pennsylvania Muscle Institute, Perelman School of Medicine, University of Pennsylvania, Philadelphia, PA, USA
- ³The Caruso Department of Otolaryngology-Head and Neck Surgery, University of Southern California, Los Angeles, CA, USA
- ⁴Department of Otorhinolaryngology, Radboud University Medical Center, Nijmegen, the Netherlands
- ⁵Department of Human Genetics, Radboud University Medical Center, Nijmegen, the Netherlands
- ⁶Department of Clinical Genetics, Amsterdam UMC, Vrije Universiteit Amsterdam, Amsterdam, the Netherlands
- Department of Otolaryngology-Head and Neck Surgery, Washington University School of Medicine, St. Louis, MO, USA
- 8These authors contributed equally
- ⁹Lead contact
- *Correspondence: epsteind@pennmedicine.upenn.edu https://doi.org/10.1016/j.devcel.2021.04.017

SUMMARY

In mammals, sound is detected by mechanosensory hair cells that are activated in response to vibrations at frequency-dependent positions along the cochlear duct. We demonstrate that inner ear supporting cells provide a structural framework for transmitting sound energy through the cochlear partition. Humans and mice with mutations in GAS2, encoding a cytoskeletal regulatory protein, exhibit hearing loss due to disorganization and destabilization of microtubule bundles in pillar and Deiters' cells, two types of inner ear supporting cells with unique cytoskeletal specializations. Failure to maintain microtubule bundle integrity reduced supporting cell stiffness, which in turn altered cochlear micromechanics in Gas2 mutants. Vibratory responses to sound were measured in cochleae from live mice, revealing defects in the propagation and amplification of the traveling wave in Gas2 mutants. We propose that the microtubule bundling activity of GAS2 imparts supporting cells with mechanical properties for transmitting sound energy through the cochlea.

INTRODUCTION

The organ of Corti is a specialized sensory epithelium unique to mammals that lines the length of the cochlear duct and is responsible for sound reception. It comprises a single row of inner hair cells (IHCs), three rows of outer hair cells (OHCs) and a variety of interspersed supporting cells that sit atop the basilar membrane. Sound waves propagate through the cochlear duct by way of fluid motion causing the basilar membrane to oscillate at frequency-dependent positions (Bekesy. 1960; Fettiplace, 2017). IHCs convert sound-induced vibrations into electrochemical signals that are transmitted to the brain along auditory nerve fibers (Yu and Goodrich, 2014; Fettiplace, 2017; Ó Maoiléidigh and Ricci, 2019). OHCs enhance the detection and discrimination of sound frequencies by amplifying basilar membrane vibrations more than 1,000-fold in a feedback loop driven by OHC electromotility (Fisher et al., 2012). In comparison with hair cells, relatively little is known about the role that supporting cells play in the transmission of mechanical vibrations across the cochlear partition.

Computational models predict that the unique geometry and cytoskeletal composition of inner ear supporting cells provides a structural framework for the exchange of forces between the basilar membrane and the apical surface of the organ of Corti (Geisler and Sang, 1995; Tolomeo and Holley, 1997; Nam and Fettiplace, 2010; Yoon et al., 2011; Liu et al., 2015; Motallebzadeh et al., 2018; Sasmal and Grosh, 2019). Nevertheless, experimental evidence in support of these models, especially from in vivo studies, is limited. It also remains unclear whether mutations in genes that selectively perturb supporting cell mechanical properties would cause hearing loss, and if so, by what means.

Pillar and Deiters cells are two types of supporting cells with intricate morphologies and cytoskeletal specializations that form strategic connections with OHCs, in keeping with their putative structural role (Pritchard, 1878; Slepecky, 1996; Soons et al., 2015). Inner and outer pillar cells form the tunnel of Corti, which separates IHCs from OHCs. The head of each inner and outer pillar cell projects laterally to contact the first and second row of OHCs, respectively (Angelborg and Engström, 1972; Slepecky and Chamberlain, 1983; Zetes et al., 2012). Deiters cells reside at the base of each OHC and extend a long phalangeal



Article



process to the reticular lamina at the apical surface of the organ of Corti into which OHCs insert their stereocilia (Slepecky, 1996; Soons et al., 2015; Fettiplace, 2017). The arrangement of OHCs and Deiters cells in a Y-shaped configuration resembles that of a braced frame used in building construction to withstand shearing forces, such as wind and seismic pressure (Nam and Fettiplace, 2010; Soons et al., 2015; Motallebzadeh et al., 2018).

A particularly striking aspect of pillar and Deiters cells is their rigid cytoskeleton composed of hundreds to thousands of microtubules organized in tightly bundled arrays that are crosslinked to actin filaments (Angelborg and Engström, 1972; Tolomeo and Holley, 1997; Sugawara et al., 2004; Szarama et al., 2012; Zetes et al., 2012). Pillar cells possess two densely packed microtubule bundles, one that runs across the pillar cell head and another that assembles parallel to the apicobasal axis (Tucker et al., 1995; Zetes et al., 2012). Deiters' cells contain microtubule bundles of lesser complexity (Sugawara et al., 2004; Zetes et al., 2012). These cytoskeletal elements bestow pillar and Deiters' cells with stiff mechanical properties (Tolomeo and Holley, 1997; Sugawara et al., 2004; Szarama et al., 2012; Zetes et al., 2012).

Microtubules are composed of polymerized α - and β -tubulin heterodimers and are generally required for cell shape, structural support, and intracellular transport in differentiated cells (Muroyama and Lechler, 2017). Not all microtubules are equivalent with respect to subunit composition, post-translational modifications, dynamic turnover, subcellular arrangement, and interactions with microtubule-associated proteins (MAPs), all of which may influence microtubule function. Previous studies have demonstrated that pillar cell microtubules are heavily detyrosinated and acetylated, which in other systems has been shown to confer stability and flexibility, respectively, in response to mechanical stresses (Slepecky et al., 1995; Saha and Slepecky, 2000; Robison et al., 2016; Portran et al., 2017; Xu et al., 2017). MAPs are also predicted to influence the mechanical properties of pillar and Deiters' cells by cross-linking microtubules to actin filaments (Tolomeo and Holley, 1997). Several candidate proteins for this cytoskeletal cross-linking activity have been proposed, but none have been functionally validated, and the identity of this factor remains elusive (Arima et al., 1986; Oshima et al., 1992; Dougherty et al., 2005; Zheng et al., 2013).

We show here that growth-arrest-specific 2 (GAS2), a protein with microtubule and actin binding domains, is expressed in pillar and Deiters' cells in a pattern that co-localizes with microtubule bundles. Gas2-mutant mice display severe hearing loss due to the disorganization and destabilization of microtubule arrays in inner ear supporting cells, resulting in a decrease in pillar cell stiffness and a buckling of Deiters' cell phalangeal processes. The reduction in pillar and Deiters' cell elastic properties alters OHC micromechanics in Gas2 mutants, causing defects in the propagation and amplification of the traveling wave, as assessed by volumetric optical coherence tomography and vibrometry (VOCTV) in live mice. Homozygous loss-of-function mutations in GAS2 were also identified in affected family members with congenital sensorineural hearing loss. Taken together, our study identifies Gas2 as a hearing loss gene required to maintain microtubule bundles in inner ear supporting cells, affording them with mechanical stiffness to transmit sound energy through the cochlea.

RESULTS

GAS2 localizes to supporting cell microtubules in the postnatal cochlea

We identified the Gas2 gene in a screen for Sonic hedgehog dependent regulators of cochlear development (Muthu et al, 2019). GAS2 is a member of a conserved family of cytoplasmic proteins that bind microtubules and actin through its GAS2 and Calponin homology domains, respectively (Figure S1A) (Brancolini et al., 1992; Zhang et al., 2011; Stroud et al., 2014). A developmental time course analysis of Gas2 expression in the inner ear of mouse embryos revealed prominent sites of staining along the medial and lateral walls of the otic vesicle and cochlear duct, marking progenitors of the sensory epithelium and stria vascularis, respectively (Figures S1B-S1F).

Robust GAS2 expression was also detected in the organ of Corti at postnatal stages, including pillar cells at postnatal day 3 (P3), and Deiters' cells at P5 (Figures 1A-1D). GAS2 staining persisted in inner and outer pillar cells as they separated from each other to form the tunnel of Corti at P7 and as they matured into adulthood (Figures 1E, 1F, 1H, and 1L). GAS2 expression was also detected in the stria vascularis, spiral prominence, and greater epithelial ridge, and was notably absent from hair cells and spiral ganglion neurons (Figure 1G).

Given the presence of dense microtubule bundles in pillar and Deiters' cells, we sought to determine whether GAS2 associates with these cytoskeletal elements by performing co-immunolabeling experiments for GAS2 and α-tubulin on cochlear preparations at P14 and P25. At these stages, the majority of pillar and Deiters cell microtubules are detyrosinated (dTyr) and acetylated (Figures S1G-S1L) (Slepecky et al., 1995; Saha and Slepecky, 2000). Extensive co-localization of GAS2 and dTyr α-tubulin staining was evident along the length of microtubule bundles in the heads of inner and outer pillar cells, as well as Deiters' cell phalangeal processes extending between rows of OHCs (Figures 1H–10). Approximately, 98% of the dTyr α-tubulin staining colocalized with GAS2 on microtubule bundles at the apical surface (head) of inner and outer pillar cells (Figures 1L-10). Co-localization of GAS2 and dTyr a-tubulin persisted in the head, body, and feet of inner and outer pillar cells into adulthood (Figures 1P-1R). These data suggested a role for GAS2 in the organization of cytoskeletal specializations in cochlear supporting cells.

Gas2^{tm1a/tm1a} mice display hearing loss

To interrogate the function of GAS2 in the inner ear we generated Gas2-mutant mice using targeted embryonic stem cells from the European Conditional Mouse Mutagenesis Program (Figure S2A) (Testa et al., 2004). Gas2^{tm1a/tm1a} mice are viable and born in the expected Mendelian ratio (Figure S3F). Loss of GAS2 expression was confirmed by immunostaining and RNA in situ hybridization on transverse sections through the cochlear duct at E11.5 (Figures S3A-S3D), as well as by western blot on protein extracts isolated from the cochlea at P0 (Figure S3E).

 ${\it Gas2}^{{\it tm1a/tm1a}}$ embryos showed no overt signs of inner ear dysmorphology (Figures S3G and S3H). Moreover, hair and supporting cells formed in the correct number and position and expressed characteristic markers of their identity (Figures S3K-S3P). Spiral ganglion neurons also appeared to innervate



Article

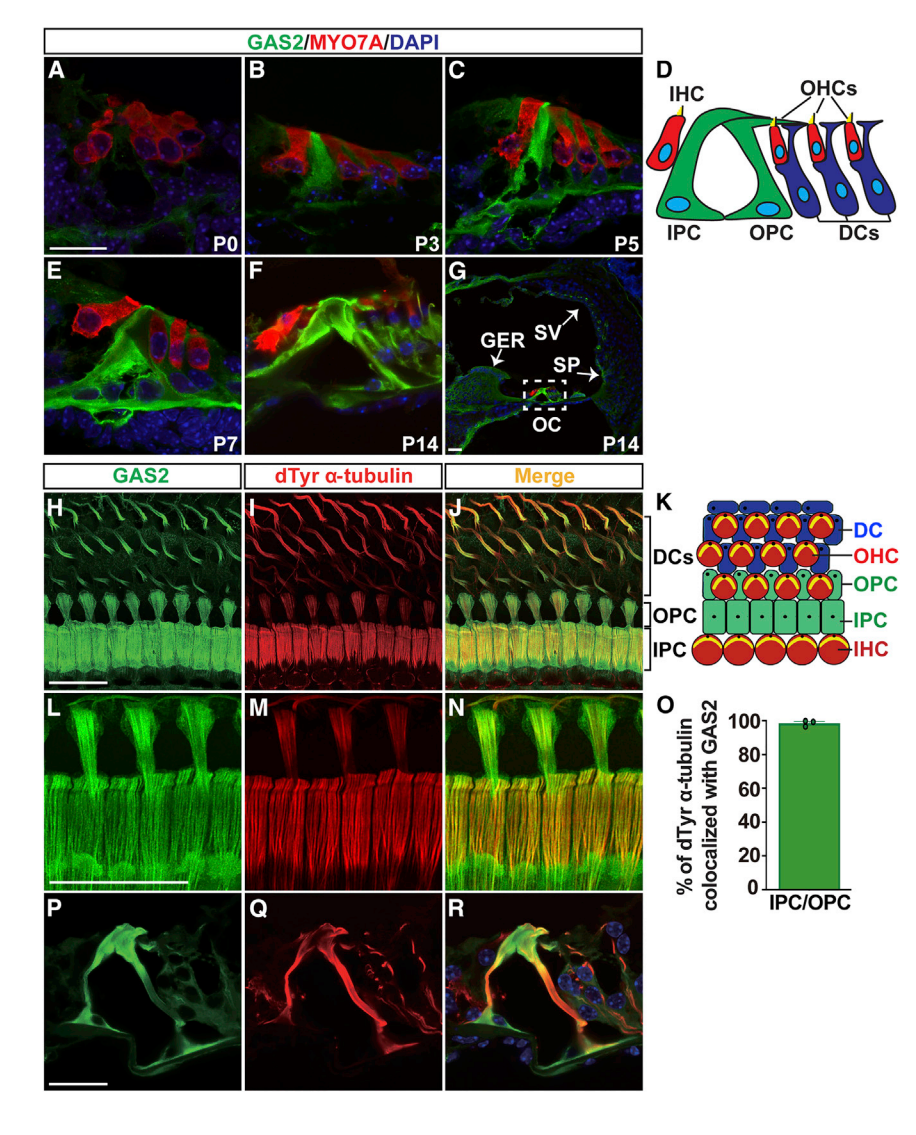


Figure 1. GAS2 localizes to supporting cell microtubules in the postnatal cochlea

(A–G) Transverse sections through the cochlea at postnatal stages stained for GAS2 (green), the unconventional myosin VIIA protein (MYO7A), which labels hair cells (red), and the 4′, 6-diamidino-2-phenylindole (DAPI) stain, which labels DNA (blue). Within the organ of Corti, GAS2 is expressed in pillar and Deiters' cells and is absent from hair cells.

(D) Schematic illustration of cell types in the organ of Corti from a transverse view.

(H–R) Co-immunostaining of GAS2 and de-tyrosinated α -tubulin (dTyr α -tubulin) on whole-mount cochlear preparations at P14 (H–J), P25 (L–N), and transverse sections through the organ of Corti at P25 (P–R). The high-resolution confocal images (Airyscan) in (L–N) show extensive co-localization of GAS2 and dTyr α -tubulin along the length of microtubule bundles in the heads of inner and outer pillar cells, as quantified in (O) (one sample t test, three inner and outer pillar cells were analyzed per sample, from three mice).

(K) Schematic illustration of cell types in the organ of Corti as viewed from the luminal surface. Scale bar, 20 μ m. Abbreviations: Deiters' cell, DC; greater epithelial ridge, GER; inner hair cell, IHC; inner pillar cell, IPC; organ of Corti, OC; outer hair cell, OHC; outer pillar cell, OPC; spiral prominence, SP; stria vascularis, SV.

loss (Locher et al., 2015). No differences in the morphology of the stria vascularis or the expression of layer specific markers were observed between Gas2^{tm1a/tm1a} and control mice (Figures S4M–S4T and S4M′–S4S′). Moreover, the loss of GAS2 did not alter endocochlear potential, the driving voltage for the hair cell mechanotransduction cur-

rent, suggesting that the cause of hearing loss in $Gas2^{tm1a/tm1a}$ mice is not due to alterations in ion homeostasis (Figure S4U).

appropriate sensory targets (Figures S3I and S3J). Cellular organization in the organ of Corti was maintained after birth in $Gas2^{tm1a/tm1a}$ mice, with no deviations in the shape of the tunnel of Corti, length of pillar cells, or distance between inner and OHCs (Figures S4A–S4L). We conclude that GAS2 is not required for cochlear morphogenesis, or for the specification of principal inner ear cell types.

We next determined whether GAS2 was necessary for hearing by measuring auditory brainstem responses (ABR) to pure tone stimuli in $Gas2^{tm1a/tm1a}$ and control mice at two months of age (P56). Gas2 mutant animals displayed significantly elevated ABR thresholds across all frequencies tested (p < 0.001, multiple t test with Holm-Sidak method, n = 6), with the most pronounced threshold shifts (\sim 50 dB) detected at higher frequencies (Figures 2A and 2B). These results indicate that $Gas2^{tm1a/tm1a}$ mice display severe hearing loss.

The expression of GAS2 in the marginal cell layer of the stria vascularis raised the possibility that defects in this tissue might be responsible for hearing loss in *Gas2* mutants. The stria vascularis is required to maintain the ionic composition of the endolymph and is frequently disrupted in genetic causes of hearing

GAS2 regulates microtubule stability and organization

With no clear indication of alterations in ion transport in $Gas2^{tm1a/tm1a}$ mice, we next examined the structure of the microtubule-rich support cells, which are another source of GAS2 expression in the postnatal cochlea. Pillar cell microtubules begin their assembly into bundles soon after birth and take approximately 14 days to fully mature. Pillar cell microtubules elongate from two organizing centers, one that forms at the lateral edge of the pillar cell head and runs parallel to the apical surface, and another that initiates more proximally in the pillar cell head and extends along the length of the body of the cell (Figure 2C) (Tucker et al., 1995).

Microtubule growth initiated properly in pillar cells of $Gas2^{tm1a/tm1a}$ mice as evaluated by dTyr α -tubulin staining at P5 (Figures 2D, 2I, and 2N). The organization of microtubules into parallel fibers with the heads of inner and outer pillar cells was similar in $Gas2^{tm1a/tm1a}$ and control mice at P12 (Figures 2E, 2J, and 2O). In contrast, small gaps in dTyr α -tubulin staining



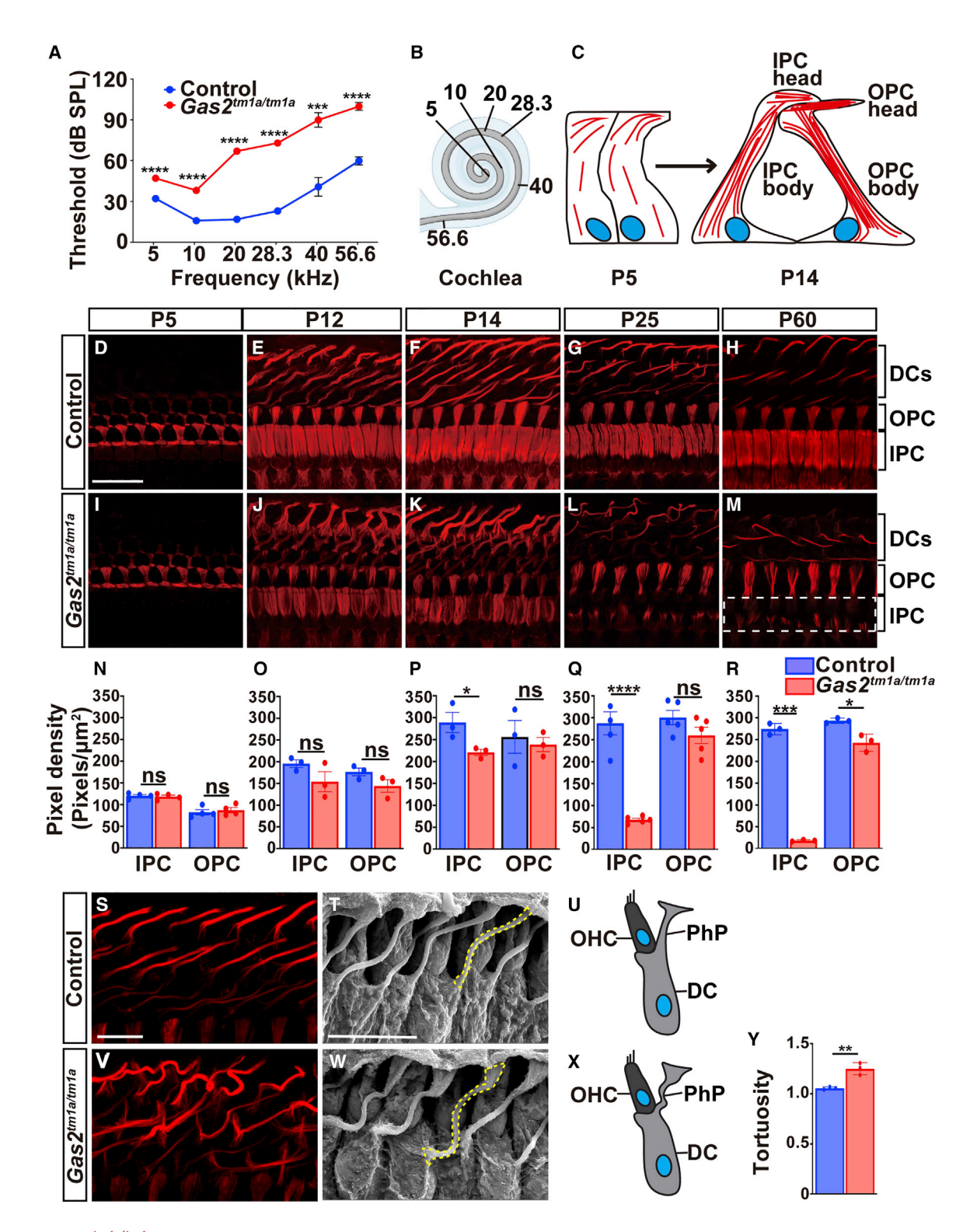


Figure 2. Gas2^{tm1a/tm1a} mice display hearing loss and defects in supporting cell microtubules

(A) ABR thresholds are elevated in Gas2^{fm1a/tm1a} (n = 6) compared with control (n = 5) mice at P56 (***p < 0.001, ****p < 0.0001, multiple t test with Holm-Sidak

(C) Illustration of microtubule bundle assembly at apical (head) and longitudinal (body) positions of inner and outer pillar cells. Microtubules are drawn in red and the nucleus in blue.

⁽B) Schematic representation of the tonotopic organization of the cochlear duct.



began to appear in the center of inner pillar cell heads from $Gas2^{tm1a/tm1a}$ mutants at P14 (Figures 2F, 2K, and 2P). This cytoskeletal defect progressed with age, such that by P25, nearly 70% of microtubules were depleted from the inner pillar cell heads of $Gas2^{tm1a/tm1a}$ mutants, compared with controls (Figures 2G, 2L, and 2Q). Almost all microtubules were lost from inner pillar cell heads at P60, with a small but significant reduction also observed in outer pillar cells (Figures 2H, 2M, and 2R). Thus, GAS2 is required to maintain microtubule bundle stability in pillar cells beginning at P14, coinciding with the onset of hearing in mice.

Deiters cell microtubules were also severely disorganized and less tightly bundled in $Gas2^{tm1a/tm1a}$ mice compared with controls, especially at P12 and P14 (Figures 2E, 2F, 2J, 2K, 2S, and 2V). Further analysis by scanning electron microscopy (SEM) revealed that the Deiters' cell phalangeal processes in $Gas2^{tm1a/tm1a}$ mutants were buckled and displayed increased tortuosity (Figures 2T, 2U, and 2W–2Y).

We further assessed the cytoskeletal ultrastructure of supporting cells by transmission electron microscopy at P25. Inner and outer pillar cells typically possess thousands of densely packed microtubules assembled in a grid like array with each microtubule surrounded by four actin filaments (Zetes et al., 2012). The number, density, and organization of pillar cell microtubules was greatly reduced in Gas2tm1a/tm1a mice, and the cross-links between microtubule and actin were mostly absent (Figures 3A-3D, 3A'-3D', 3G-3J, 3M-3P, and 3S-3V). Deiters' cell microtubules were also disorganized in ${\it Gas2}^{{\it tm1a/tm1a}}$ mice, but the total number did not differ from controls, and yet, microtubule density was still reduced due to the expanded area of the phalangeal process (Figures 3E, 3F, 3E', 3F', 3K, 3L, 3Q, 3R, 3W, and 3X). These results demonstrate that GAS2 is required to organize the cytoskeletal ultrastructure of pillar and Deiters' cells likely through the formation of microtubule-actin cross-links.

Supporting cells are less stiff in the absence of GAS2

To assess the mechanical consequences of Gas2 loss, we developed a cochlear explant assay that recapitulates the timing of microtubule destabilization and measured supporting cell stiffness by atomic force microscopy (Figures 4A–4C). Cochlear explants isolated from control and $Gas2^{tm1a/tm1a}$ mice at P9 and grown for one day in culture (P9 + 1DIC) showed little to no difference in stiffness properties across pillar cells and OHC rows, including regions between OHCs where Deiters' cell phalangeal processes contact the reticular lamina (Figures 4D–4G). Whereas stiffness measurements increased over time from P9+1DIC to P9+5DIC across pillar and OHC rows in control explants, consistent with the normal gain in microtubule density that occurs in postnatal animals, no such increase was observed

in Gas2^{tm1a/tm1a} samples (Figures 4D–4G). These data indicate a critical role for GAS2 in providing cochlear supporting cells with stiff mechanical properties.

OHC amplification is dependent on GAS2 in supporting cells

How might alterations in supporting cell stiffness impact auditory function? Given that both pillar and Deiters cells provide mechanical support to OHCs and that amplification of basilar membrane vibrations by OHCs is required for hearing, we evaluated Gas2^{tm1a/tm1a} mice for defects in OHCs. A small but progressive loss of OHCs was observed in Gas2tm1a/tm1a mice, resulting in a 10% decrease in OHC number by P60 (Figures 5A-5K). This minor reduction in OHCs is unlikely to account for the hearing loss detected in Gas2^{tm1a/tm1a} mice (Hamernik et al., 1989; Chen and Fechter, 2003; Chen et al., 2008). Moreover, SEM images of OHCs and IHCs showed no obvious differences in stereocilia bundle morphology between Gas2tm1a/tm1a and control mice at P60 (Figures 5L-50). Nevertheless, we did detect a significant upregulation in Caveolin 2 (CAV2) expression in OHCs from Gas2^{tm1a/tm1a} mice at P25 and P60 (Figures S5A-S5I). Caveolins are plasma membrane proteins and major constituents of lipidrich caveolae that, among their many proposed roles, act as sensors of mechanical stress in a variety of cell types, including OHCs (Sinha et al., 2011; Anzai et al., 2015; Echarri et al., 2019). We suspect that the cytoskeletal defects in supporting cells may impose undue mechanical stress on OHCs, thus interfering with their ability to amplify basilar membrane vibrations in $Gas2^{tm1a/tm1a}$ mice.

We next measured distortion product otoacoustic emissions (DPOAE), a sensitive readout of OHC amplification and organ of Corti mechanics (Kemp, 2002). DPOAEs from control mice showed amplitudes of 20 to 40 dB above the noise floor at f2 frequencies between 10 and 30 kHz, whereas DPOAEs were significantly reduced by 10 to 20 dB in $Gas2^{tm1a/tm1a}$ mice (Figure 5P). This defect in cochlear function does not appear to be attributed to alterations in the OHC motor protein Prestin, which continues to be expressed in $Gas2^{tm1a/tm1a}$ mice (Figures S5J–S5O). Based on these findings, we stipulate that the reduction in supporting cell stiffness in $Gas2^{tm1a/tm1a}$ mice interferes with the OHC mediated active process, resulting in hearing loss.

To confirm that the change in cochlear mechanics was indeed attributed to the loss of GAS2 in supporting cells we generated conditional *Gas2*-knockout mice (*cGas2*) by first converting the *Gas2*^{tm1a} allele into a *Gas2*^{loxp} allele and then crossing these mice to an inducible *Sox2*^{CreER/+} line (Figures S2A–S2C). *cGas2*-knockout mice (*Sox2*^{CreER/+}; *Gas2*^{loxp/loxp}) that were administered tamoxifen at early postnatal stages displayed selective loss of GAS2 expression in supporting cells and highly similar inner ear pathology and auditory dysfunction as

(D–M) Time course analysis of dTyr α -tubulin immunostaining on whole-mount cochlear preparations from control and $Gas2^{tm1a/tm1a}$ mutants. The heads of inner pillar cells show a progressive destabilization of microtubule bundles that are almost completely absent at P60 (dotted white box). (N–R) Quantification of dTyr α -tubulin pixel density in pillar cells from control and $Gas2^{tm1a/tm1a}$ mice presented as mean \pm SEM (*p < 0.05, ****p < 0.0001, two-tailed t test, six cells were analyzed per mouse, from a minimum of three mice, ns, not significant).

(S and V) Whole-mount dTyr α -tubulin immunostaining of cochlear preparations from control and $Gas2^{tm1a/tm1a}$ mice at P25 showing microtubule disorganization in Deiters' cell phalangeal processes. SEM images (T and W) and schematic illustrations (U and X) of Deiters' cells from control and $Gas2^{tm1a/tm1a}$ mice at P25 showing increased tortuosity of phalangeal processes (yellow dashed line) quantified in (Y) (**p < 0.01, two-tailed t test; four cells were analyzed per sample, n = 3, error bars represent SEM). Scale bar, 20 μ m (D), 10 μ m (S), 10 μ m (T). Abbreviations: Deiters' cell, DC; inner pillar cell, IPC; outer pillar cell, OPC; outer hair cell, OHC: phalangeal process. PhP.



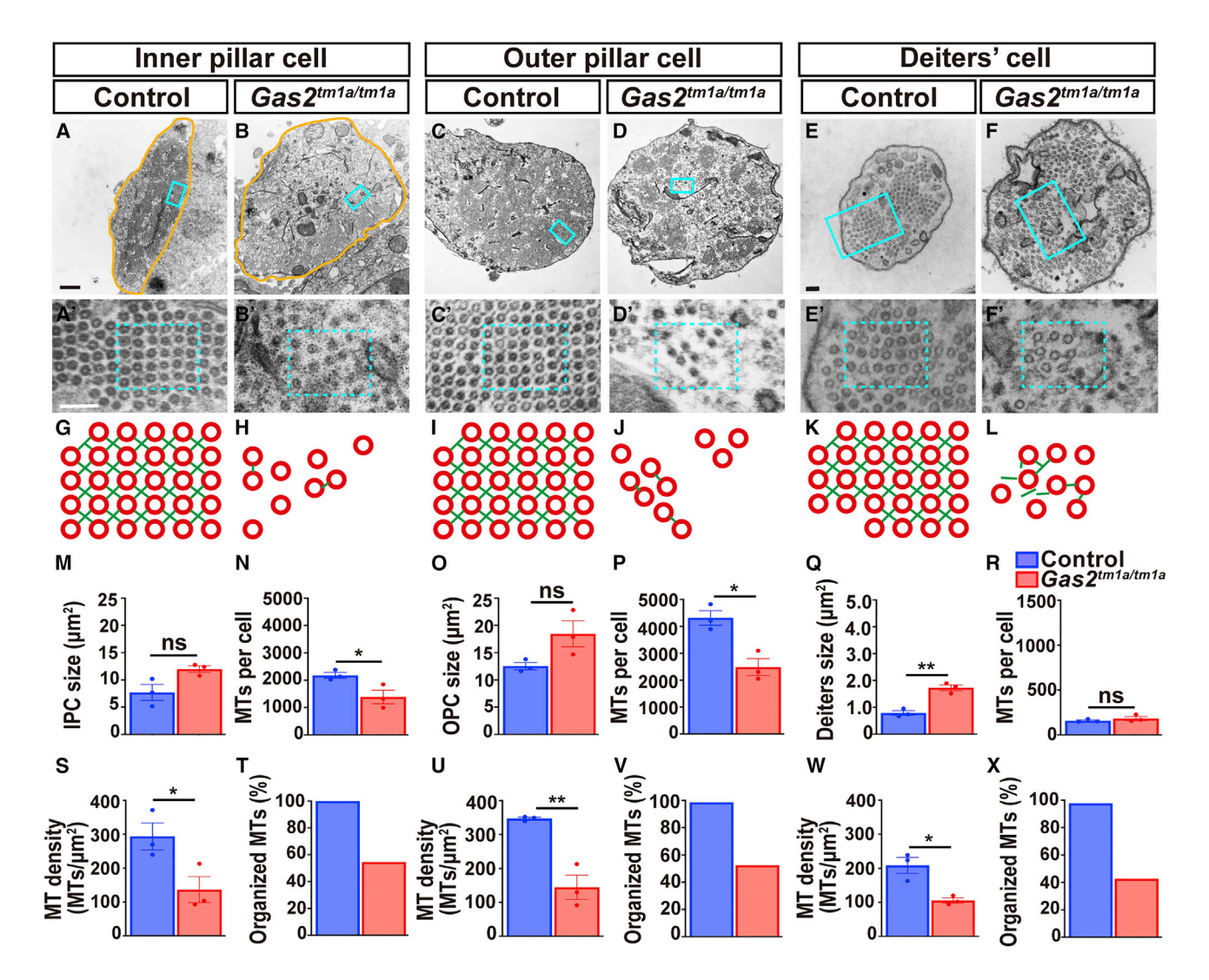


Figure 3. Cytoskeletal ultrastructure is dependent on GAS2

(A-F) Transmission electron micrographs through the body of inner and outer pillar cells, and a Deiters' cell phalangeal process from control and Gas2^{tm1a/tm1a}

(A'-F') Enlargement of boxed areas from (A-F).

(G-L) Schematic illustration of cytoskeletal organization corresponding to boxed regions in (A'-F'). Note the disorganization and destabilization of microtubule arrays and disruption of actin (green) and microtubule (red) cross-links in Gas2^{tm1a/tm1a} mice.

(M-X) Quantification of cell size, microtubule number, and density and organization in pillar and Deiters' cells presented as mean ± SEM. (*p < 0.05, **p < 0.01, two-tailed t test, three cells were analyzed per sample, n = 3 samples, ns, not significant) Scale bars, 500 nm (A), 100nm (A', E, and E').

the constitutive Gas2^{tm1a/tm1a} mutants (Figures S6A-S6K). Sox2^{CreER/+} is also active in hair cells at early postnatal stages (Walters et al., 2015). However, GAS2 is not expressed in hair cells at any of the postnatal stages examined (Figures 1 and S6), alleviating concern that Sox2^{CreER} mediated recombination in hair cells might confound these results. Therefore, we conclude that the postnatal expression of GAS2 in supporting cells is required for OHC amplification.

Transmission of sound-evoked vibrations is impaired in Gas2^{tm1a/tm1a} mice

If pillar and Deiters cells act as structural scaffolds to support the mechanical properties of the organ of Corti, then destabilization of their cytoskeletal network should interfere with the transfer of mechanical vibrations through the cochlear partition. To formally test this premise, we measured vibratory responses to sound in live mice using VOCTV (Lee et al., 2015). First, we imaged the apical turn of the mouse cochlea in vivo. The cochlear anatomy of wild-type mice imaged using VOCTV has been thoroughly documented (Gao et al., 2014; Lee et al., 2015; Dewey et al., 2018, 2019; Kim et al., 2018). We found that the cochlear anatomy of ${\it Gas2^{tm1a/tm1a}}$ mice appeared grossly normal (Figures 6A and 6B). In particular, the morphology of the three cochlear scalae, Reissner's membrane (RM), the basilar membrane (BM), and the tectorial membrane (TM) were all indistinguishable from what is found in wild-type mice.

Vibratory responses to sound stimuli were then measured from the BM within the apical turn to produce tuning curves.



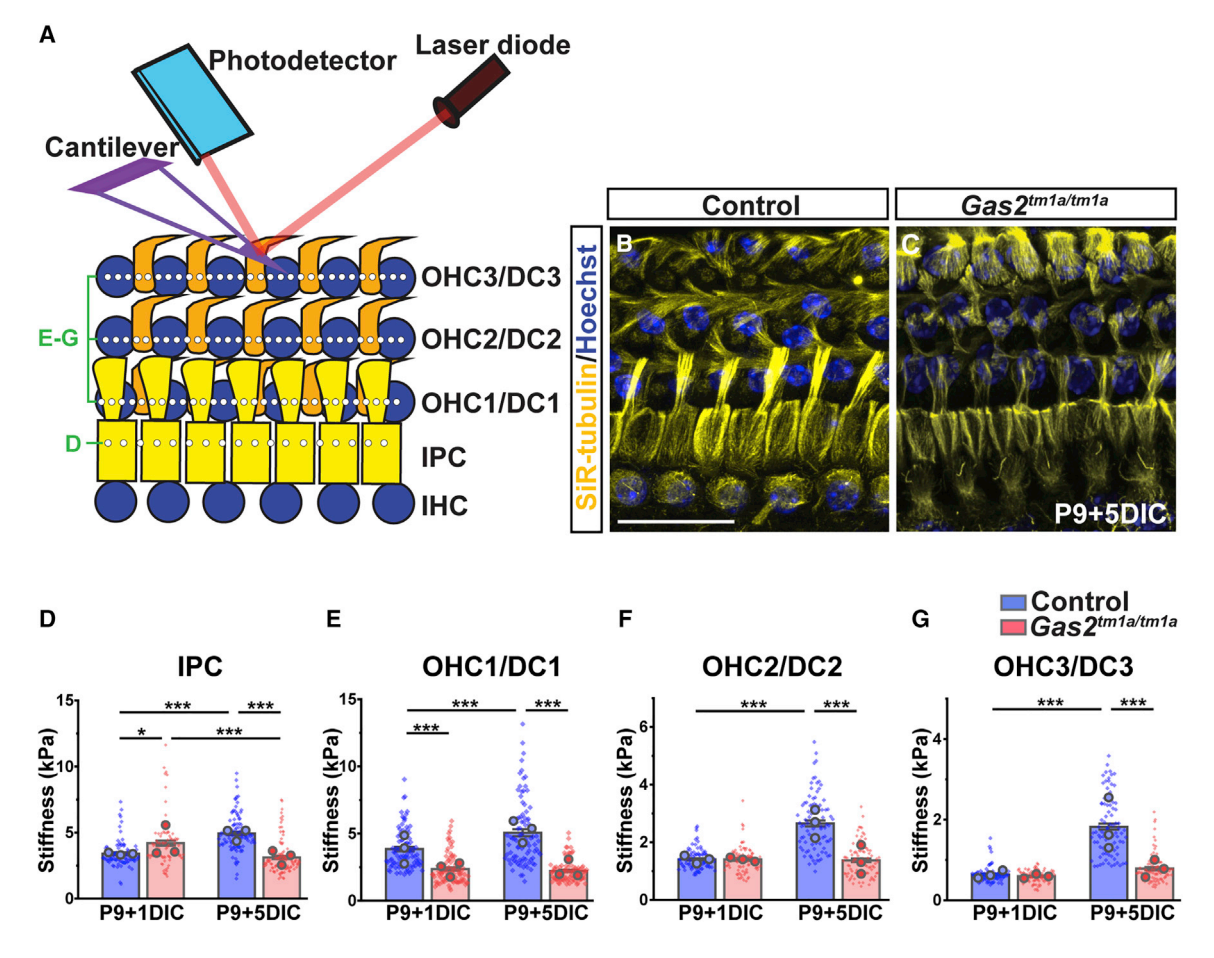


Figure 4. Supporting cells are less stiff in the absence of GAS2

(A) Illustration of experimental approach for measuring supporting cell mechanical properties by AFM. (B and C) Cochlear explants isolated from Gas2^{tm1a/tm1a} mice at P9 and grown for 5 days in culture (DIC) recapitulate supporting cell microtubule defects when compared with control mice as indicated by SiR tubulin (yellow) and Hoechst (blue) staining. Scale bar, 20 µm.

(D-G) Quantification of stiffness in pillar cells (D) and individual OHC/Deiters cell (DC) rows (E-G). The data are presented as mean ± SEM of 30 measurements (diamonds) at 2-µm increments along each cell row, which was repeated for all rows in three independent cochlear samples (mean for each cochlea is shown as large circle) (*p < 10^{-3} , ***p < 10^{-6} , two-way ANOVA on cellular measurements with post hoc Bonferroni comparison, factors of genotype and DIC).

Data from one representative control and Gas2^{tm1a/tm1a} mouse are shown (Figures 6C and 6D). The sensitivity was calculated by dividing the displacement magnitude by the intensity of the sound stimulus. Control mice had the typical pattern of nonlinear gain with sharper tuning and higher sensitivity for low intensity stimuli, termed cochlear amplification. While the same pattern was found in Gas2tm1a/tm1a mice, the amount of gain was lower. In fact, vibratory responses to 10- and 20-dB sound pressure level (SPL) stimuli were below the noise floor in Gas2^{tm1a/tm1a} mutants, whereas they were easily measured in control mice. Post-mortem, within each mouse, the sensitivity curves all overlapped, demonstrating the expected loss of cochlear amplification in both controls and mutants. In both live and dead mice, the vibration of the BM exhibited a progressive phase lag as the sound frequency was increased, consistent with traveling wave propagation (Figures 6C and 6D).

We then averaged the vibratory responses from nine control and eight Gas2^{tm1a/tm1a} mutant mice (Figures 6E and 6F). Within each cohort, the vibratory characteristics appeared quite similar

as evidenced by the small SEM. The characteristic frequency (CF) of the measurement location, which is the frequency of maximal vibration to the lowest intensity stimuli, was similar between the cohorts (mean \pm SEM for the control and $Gas2^{tm1a/tm1a}$ mutant were 8.8 \pm 0.1 kHz and 8.4 \pm 0.11 kHz, respectively; p = 0.21). However, the reduced gain in the Gas2^{tm1a/tm1a} mutants was again notable by the lack of responses to 10- and 20-dB SPL stimuli.

Next, we converted the averaged displacement data to sensitivity from the two cohorts, overlapped the responses, and assessed for differences between them (Figures 6G and 6H). Several notable features were observed. First, live Gas2^{tm1a/tm1a} mutants were found to have lower gain than live control mice. This was quantified as a difference in the change in sensitivity between 40-80 stimuli at the CF (p = 0.003). Second, vibratory sensitivities to lower frequency stimuli were more level- and frequency-dependent for live control than live Gas2^{tm1a/tm1a} mice. such that the onset of the nonlinearity was at \sim 0.5CF for the control whereas this was ${\sim}0.7\text{CF}$ for the $\textit{Gas2}^{\textit{tm1a/tm1a}}$ mutant. We



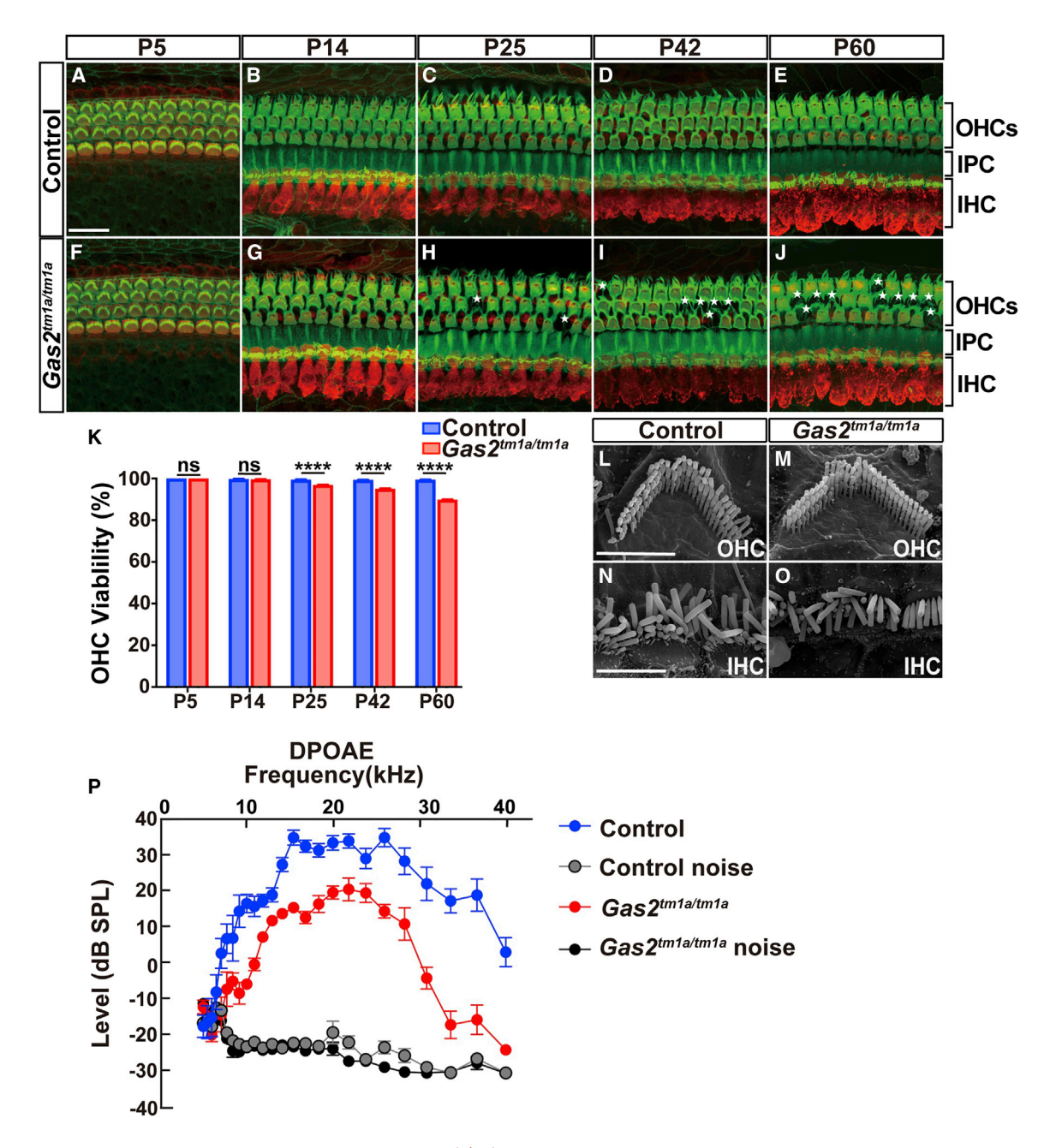


Figure 5. Outer hair cell function is compromised in Gas2^{tm1a/tm1a} mice

(A-J) Time course analysis of MYO7A (red) and F-actin (green) immunostaining on whole-mount cochlear preparations from control and Gas2^{tm1a/tm1a} mice (n = 3 per timepoint). A small number of OHCs are lost over time (indicated by asterisk). Scale bar, 20 µm. (K) Quantification of OHC viability (****p < 0.001, Fisher's exact test, ns, not significant).

(L-O) SEM images of OHCs (L and M) and IHCs (N and O) from control and Gas2^{tm1a/tm1a} mice at P60, showing normal stereocilia morphology. Scale bars, 3 µm (L)

(P) DPOAEs are significantly reduced in Gas2^{tm1a/tm1a} (n = 5) compared with control mice (n = 6) at P56 (p < 0.05, multiple t test with Holm-Sidak method). Abbreviations: inner hair cell, IHC; inner pillar cell, IPC; outer hair cells, OHCs; outer pillar cell, OPC.

quantified this as a difference in the gain at 0.7 CF (p = 0.01). Thus, the frequency range over which cochlear amplification occurs on the BM is reduced in Gas2 mutants. Third, there was no difference in the sharpness of the tuning curves between the genotypes. We tested for this by calculating the Q_{10dB}, the frequency at the peak divided by the bandwidth at 10 dB below the peak. We compared the Q_{10 dB} for live and dead mice to determine whether this was related to cochlear amplification; however, the results demonstrated no significant differences (live, p = 0.44; dead, p = 0.56). Fourth, the phase slope at the CF was steeper in Gas2^{tm1a/tm1a} compared with control mice (p = 0.0013). The rate of change of the phase with respect to

Article

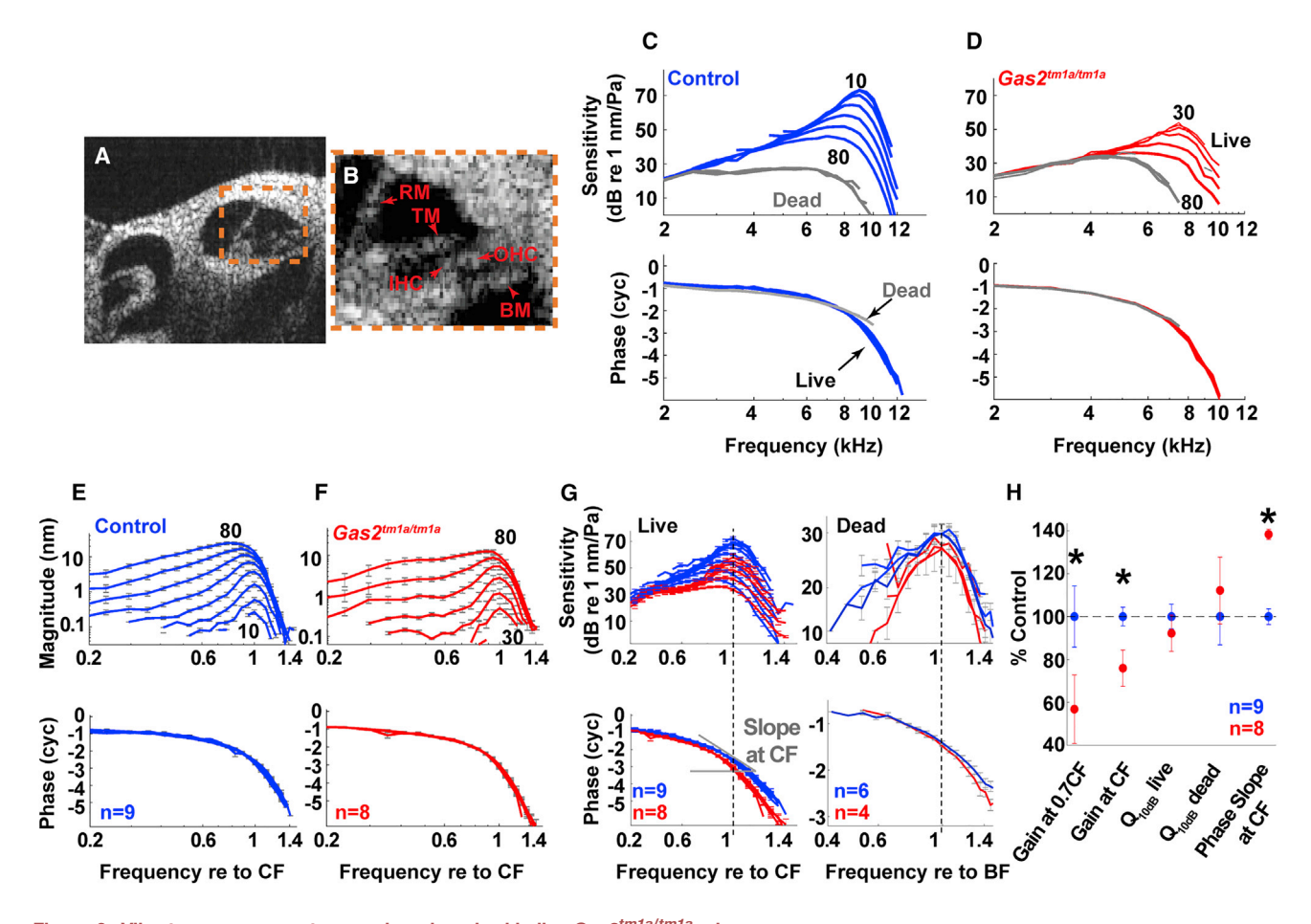


Figure 6. Vibratory responses to sound are impaired in live ${\sf Gas2}^{tm1a/tm1a}$ mice

(A) Cross-sectional image of the apical cochlear duct of a mouse obtained with VOCTV.

(B) Enlargement of organ of Corti (boxed region in A); BM, basilar membrane; IHC, inner hair cell; OHC, outer hair cell; RM, Reissner's membrane; TM, tectorial membrane.

(C and D) BM sensitivity and phase for one control (blue) and one $Gas2^{tm1a/tm1a}$ (red) mouse. The numbers indicate the highest and lowest stimulus intensities that produced measurable vibratory responses. Post-mortem data (60–80 dB SPL) are in gray.

(E and F) Average displacements and phases of the BM motions for control (n = 9) and $Gas2^{tm1a/tm1a}$ (n = 8) mice. Frequencies are normalized to the CF of each individual mouse and error bars indicate the SFM

(G) The averaged vibratory sensitivity and phases of BM motion for live and dead mice are compared in control (blue) and $Gas2^{tm1a/tm1a}$ (red) mice. The frequencies are normalized to the corresponding CF and best frequency (BF) for live and dead data, respectively. Data from live mice show that $Gas2^{tm1a/tm1a}$ mutants have less amplification near CF and sharper phase change with increasing frequency. Data from dead mice (80 dB SPL) also show sharper phase change for $Gas2^{tm1a/tm1a}$ mutants.

(H) Mean values of sensitivity change from 40 to 80 dB SPL at 0.7CF, CF, and Q_{10dB} for live (40 dB SPL stimuli) and dead (80 dB SPL stimuli) mice, and phase slope (for 40 dB SPL at the CF) as a percentage of the appropriate control mean. Asterisks denote p < 0.05.

the frequency corresponds to the traveling wave group delay. This result indicates that the traveling wave propagates more slowly near the CF in $Gas2^{tm1a/tm1a}$ mutant mice and that there is less longitudinal coupling. This was found in both the live and dead conditions (Figure 6G).

Whole-exome sequencing identifies *GAS2* mutations in a family with hearing loss

To determine if *GAS2* is associated with hearing loss in humans, we screened families with unsolved cases of hereditary sensorineural hearing loss for mutations in *GAS2*. Four male siblings, born from consanguineous parents of Somalian descent, presented with early onset high-frequency hearing loss at the Department of Clinical Genetics, Amsterdam University Medical Center

(Figure 7A). Two brothers (V.6 and V.7) were diagnosed with hearing loss at birth and two others (V.2 and V.5) were diagnosed at one year of age. All affected subjects had delayed speech and language development. Medical history did not indicate any non-genetic causes of hearing impairment. Physical examinations did not reveal any abnormalities or dysmorphic characteristics.

Audiometry showed symmetrical bilateral (high-frequency) hearing loss in subjects V.2 and V.5–V.7 (Figures 7B and S7A). Hearing in subject V.2 showed mild progression over time for the lower frequencies. Subjects IV.2, V.3, and V.4 had normal hearing for their age (Table S2). Oto-acoustic emissions were present in unaffected subjects and absent in affected subjects, except for transient evoked emissions in subject V.7 (Table S2). Click-evoked automated brainstem response and speech

Article



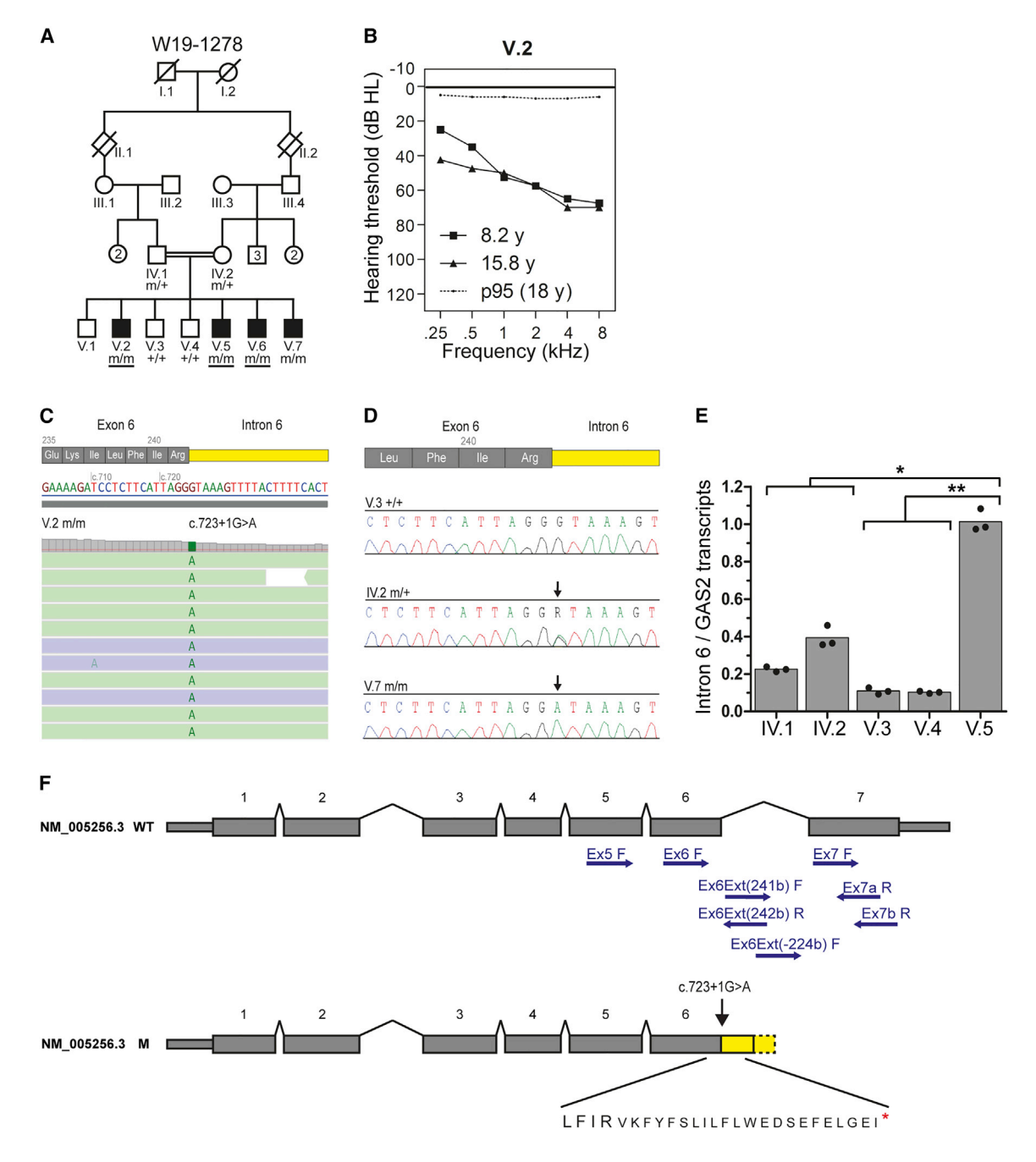


Figure 7. Human GAS2 mutations associate with hearing loss

- (A) Pedigree of family W19-1278. WES was performed in subjects with an underlined genotype. M, mutant GAS2 c.723+1G>A; +, wild type.
- (B) Average air conduction thresholds for both ears from subject V.2 measured at 8.2 and 15.8 years of age (y). The dotted line represents the 95th percentile of age- and sex-specific hearing level at the age of 18 years. This is the lowest age for which the ISO 7029:2017 standard can be applied. dB HL, decibel hearing level: kHz_kilohertz
- (C) Analysis of WES paired-reads demonstrating a homozygous single nucleotide variant, GAS2 c723+1G>A, in subject V.2.
- (D) Sequences of exon6-intron6 boundaries amplified from genomic DNA of unaffected subjects V.3 and IV.2 and affected subject V.7. Arrows indicate the position of the c723+1G>A variant.
- (E) Bar graph showing the genotype dependence of intron 6 retention. Depicted are the ratios of relative levels of transcripts with intron 6 retention and relative levels of total GAS2 transcript. The dots represent the means of three independent experiments performed in triplicate (*p value = 0.021; **p value = 0.013). No statistically significant difference (p value = 0.137) was observed between the parents and the unaffected offspring.
- (F) Schematic representation of GAS2 transcript NM_005256.3 and the effects of the c723+1G>A variant on exon 6 splicing. The positions of primers used in RT-PCR are indicated (see Table S1 for primer combinations and sequences). Predicted amino acid sequence, including in-frame stop codon (red asterisk), resulting from intron 6 retention is shown below the mutant transcript. Abbreviations: wild type, WT; mutant, M.



audiometry in affected subjects did not indicate retrocochlear pathology. Vestibular testing in the affected subjects V.2 and V.5-V.7 revealed normal vestibular function, comparable with that in the unaffected subjects V.3 and V.4.

Medical genetic testing revealed no pathogenic variants or copy number variants (CNVs) in 173 genes on the hereditary hearing loss gene panel. Subsequently, an "open-the-exome" analysis was carried out to identify variants that were shared by subjects V.2, V.5, and V.6. This revealed a single rare homozygous variant, a nucleotide substitution in a canonical splice donor site in intron 6 of GAS2 [MIM 602835]: Chr11(GRCh37/hg19): g.22777500G>A; NM_005256.3:c.723+1G>A; p.? (Figure 7C). The GAS2 variant segregated in the homozygous state with hearing loss in the family (Figures 7A and 7D). The unaffected parents were heterozygous for the GAS2 variant (Figures 7A and 7D). The variant is not reported in gnomAD (v.2.1.1) or the in-house wholeexome sequencing (WES) dataset (>15,000 exomes) at Radboud University Medical Center. No further (likely) pathogenic GAS2 variants were identified in WES data of ~800 index cases with hearing loss. Two compound heterozygous variants in TMPRSS4 were also found to segregate with hearing loss in the family; however, TMPRSS4 is not known to function in the inner ear and has very low expression in the cochlea (gEAR portal, https://umgear. org/) and was therefore not considered further.

The effect of the c.723+1G>A variant on GAS2 splicing was evaluated by RT-PCR on RNA isolated from EBV-transformed cells from the parents (IV.1 and IV.2), unaffected siblings (V.3 and V.4), and affected subject (V.5) (Figure S7B). Almost no wild-type splicing was observed between exons 6 and 7 in subject V.5, resulting in retention of intron 6 (Figure S7B). The proportion of GAS2 transcripts that retained intron 6 was significantly higher in affected subject compared with unaffected siblings, with intermediate levels observed in the heterozygous parents (Figure 7E). The mutant GAS2 transcripts are predicted to encode for a truncated GAS2 protein that terminates translation prematurely within the GAS2 domain due to the presence of an in-frame stop codon (TGA) at position c.723+67-69 (Figure 7F). These results, supported by our findings in mice, identify mutations in GAS2 as a cause of hearing loss.

DISCUSSION

Our study identifies GAS2 as a cytoskeletal regulatory protein that provides cochlear supporting cells with stiffness properties for transmitting mechanical forces through the cochlear partition in response to sound. We demonstrate that GAS2 is a structural MAP required for the organization and stabilization of microtubule bundles in pillar and Deiters cells and the formation of cross-links with actin filaments. This GAS2 dependent microtubule bundling activity equips pillar and Deiters cells with a rigid but flexible cytoskeletal framework for transferring forces from the BM to the reticular lamina, which are then amplified by OHCs. Consequently, Gas2 mutations in mice and humans cause hearing loss through a mechanism that alters the way the traveling wave propagates along the cochlea.

Physiological role of GAS2 in hearing

OHCs generate force to selectively amplify BM traveling waves that peak at characteristic frequencies along the cochlear duct

(Fisher et al., 2012). Our work indicates that, in both the live and dead conditions, sound-induced vibration in one area of the BM causes the more apical regions to move less in ${\it Gas2}^{{\it tm1a/tm1a}}$ compared with control mice. In other words, there is less longitudinal coupling in Gas2 mutants. This conclusion stems mostly from the difference in the phase slopes between the two genotypes. The steeper phase slope in dead Gas2 mutant compared with dead control mice means that the traveling wave is slower, a feature of reduced longitudinal coupling. In the live condition, this additionally manifests as a smaller frequency range over which cochlear amplification occurs (i.e., the 0.7CF versus 0.5CF difference). One feature of reduced longitudinal coupling that we did not detect was sharper tuning, which would have been indicated by a larger Q_{10dB} in $Gas2^{tm1a/tm1a}$ mutants. This is not surprising given that cochlear tuning includes multiple components beyond supporting cell stiffness, such as the degree of amplification and the mechanical properties of the BM, TM, and surrounding cochlear fluids (Legan et al., 2000; Robles and Ruggero, 2001; Russell et al., 2007; Karavitaki and Mountain, 2007; Gao et al., 2014; Dewey et al., 2019; Nankali et al., 2020).

Nevertheless, compared with Prestin-/- mutants that lack OHC electromotility, the fundamental mechanism of power production continues to exist in Gas2tm1a/tm1a mice, albeit at reduced capacity (Figures 6C-6F) (Liberman et al., 2002; Dallos et al., 2008; Gao et al., 2014). Thus, our data show that the supporting cell dysfunction in Gas2 mutant mice reduces longitudinal coupling so that less OHCs are involved in amplifying the traveling wave. An additional explanation for the defects in cochlear amplification is that the reduced stiffness of Deiters' cell phalangeal processes fails to buffer OHCs from compressive forces. This premise is consistent with our observation that OHCs from Gas2^{tm1a/tm1a} mice display increased mechanical stress (Figures S5A-S5I). Similarly, the altered mechanical impedance of the organ of Corti may reduce power transfer from the OHC to the cochlear partition, thus impeding the feedback loop that drives cochlear amplification (Fisher et al., 2012). Finally, another possibility is that the reduced stiffness of the Deiters' cell phalangeal processes impacts the feedforward mechanism, a hypothetical role for these cells (Geisler and Sang, 1995; Yoon et al., 2011). These pathogenic mechanisms are not mutually exclusive and either one or all might explain the reduction in DPOAEs in mice with constitutive or conditional mutations in Gas2.

Our data also provide experimental evidence in favor of predictions made from mathematical models of cochlear micromechanics (Nam and Fettiplace, 2010; Yoon et al., 2011; Liu et al., 2015; Motallebzadeh et al., 2018; Sasmal and Grosh, 2019). These models emphasize the importance of the organ of Corti cytoarchitecture, including the Y-shaped configuration of Deiters' cells and OHCs for cochlear amplification. Taken together, these data lend further support to our conclusion that the distortion of Deiters' cells hinders cochlear amplification in Gas2 mutant mice and contributes to hearing loss.

GAS2 is required for cytoskeletal cross-links in cochlear supporting cells

In addition to demonstrating the physiological importance of the supporting cell cytoskeleton for hearing, our data reveal that the

Article



organization and stabilization of the dense microtubule networks in pillar and Deiters' cells are dependent on GAS2-mediated cross-linking activity. In the absence of GAS2, supporting cell microtubules are no longer tethered to actin, resulting in their disarray over time. Our finding that stiffness was reduced in pillar and Deiters cells from Gas2 mutants prior to the exacerbation of the cytoskeletal phenotype emphasizes the importance of this cross-linking activity for supporting cell mechanical properties, in agreement with theoretical models (Tolomeo and Holley, 1997).

Similar cytoskeletal disorganization has been described in neurons upon the loss of MAPs, especially those with cross-linking activity (Sanchez-Soriano et al., 2009; Ka and Kim, 2016; Hahn et al., 2019; Bodakuntla et al., 2019). Interestingly, the GAS2 family member, GAS2L1, also regulates actin-microtubule cross talk during axonal maturation (van de Willige et al., 2019). Association of the GAS2 domain with microtubules causes disinhibition of the CH domain, allowing GAS2L1 to simultaneously interact with actin filaments. The GAS2L1-dependent stabilization of F-actin filaments in rat hippocampal neurons was shown to promote axon branching, while restricting outgrowth. Thus, GAS2 family members constitute a group of structural MAPs with cytoskeletal organizing properties that influence diverse cellular and physiological processes.

While pillar and Deiters' cells are both dependent on GAS2 for the organization of microtubules into grid like arrays, only pillar cell microtubules break down over time. It is unclear what accounts for this difference. MAPs regulate microtubule dynamics through a variety of means, including the stimulation of microtubule growth, the inhibition of microtubule depolymerization, or the shielding of microtubules from severing enzymes (Bodakuntla et al., 2019). It is conceivable that the differential expression or activity of factors regulating microtubule dynamics accounts for the cell-type-specific differences in microtubule stability. Interestingly, the pillar and Deiters' cell microtubules that persist in Gas2 mutants remain detyrosinated and acetylated. Therefore, not only are these α-tubulin post-translational modifications not dependent on GAS2 for their deposition, but they do not appear to be responsible for the loss of pillar cell microtubules, despite their known roles in microtubule stability and flexibility (Robison et al., 2016; Portran et al., 2017; Xu et al., 2017). It is also possible that since pillar cells serve as a hinge point during BM vibrations, they are subject to deformation, causing microtubules to break in the absence of GAS2 (Nilsen and Russell, 2000; Fridberger et al., 2002; Chan and Hudspeth, 2005; Ni et al., 2016).

Human GAS2 mutations associate with hearing loss

The significance of our study is further heightened by the discovery that GAS2 mutations segregate with hearing loss in a human pedigree. It is intriguing that hearing loss was more pronounced at higher frequencies in both humans and mice with GAS2 mutations, suggesting a common pathogenic mechanism. In addition to hearing loss, female Gas2 mutant mice also exhibit reduced fertility (York et al., 2016). The combination of hearing loss in both sexes and reduced fertility in females has been described in humans with Perrault syndrome, a rare recessive disorder with a genetically heterogeneous etiology (Chatzispyrou et al., 2017; Newman et al., 2018; Tucker et al., 2020). The cause of Perrault syndrome remains unidentified in 60% of cases, suggesting the likely involvement of additional genes (Newman et al., 2018). GAS2 is a plausible candidate given the phenotypic overlap between Gas2 mutant mice and Perrault syndrome patients. However, since no affected females were present in the pedigree in our study, further investigation of exomes from genetically unconfirmed cases of Perrault syndrome will be needed to determine if mutations in GAS2 are linked to this condition.

Limitations of the study

While the body of evidence provided in this study supports our principal conclusion that supporting cell stiffness is required for cochlear mechanics, the precise mechanism by which GAS2 mediates cytoskeletal cross-linking activity in pillar and Deiters' cells remains uncertain. Further experimentation will be needed to determine if the microtubule arrays are directly cross-linked to actin by GAS2, or whether they occur through interactions with additional MAPs. Furthermore, we cannot rule out the possibility that GAS2 expression in other inner ear cell types may also play a role in auditory function. For instance, interrogation of singlecell RNA-seq datasets in the gEAR portal (https://umgear.org/) indicates that Gas2 is also expressed in cochlear hair cells, albeit at a level that falls below our detection by immunostaining or in situ hybridization. The generation of conditional mutants that selectively delete Gas2 in hair cells will be needed to determine if sensory cell types also require GAS2 for hearing.

STAR*METHODS

Detailed methods are provided in the online version of this paper and include the following:

- KEY RESOURCES TABLE
- RESOURCE AVAILABILITY
 - Lead contact
 - Materials availability
 - Data and code availability
- EXPERIMENTAL MODEL AND SUBJECT DETAILS
 - Mouse lines
 - Human subjects
- METHOD DETAILS
 - In situ hybridization
 - Inner ear paint fill
 - Whole mount cochlear preparations
 - Immunohistochemistry
 - Western blot
 - O Auditory Brainstem Response
 - O Distortion product otoacoustic emissions
 - Endocochlear potential recording
 - Scanning electron microscopy (SEM)
 - Transmission electron microscopy (TEM)
 - O Cochlear explant culture
 - Atomic Force Microscopy (AFM)
 - Cochlear vibration measurements
 - DNA sequencing and variant identification
 - O GAS2 mutations and family data
 - Clinical evaluation
 - O RT-PCR
 - O QPCR
- QUANTIFICATION AND STATISTICAL ANALYSIS



SUPPLEMENTAL INFORMATION

Supplemental information can be found online at https://doi.org/10.1016/j.devcel.2021.04.017.

ACKNOWLEDGMENTS

We thank Dr. Jean Richa and his staff at the Transgenic and Chimeric Mouse Facility (Perelman School of Medicine, University of Pennsylvania) for assistance with transgenic mouse production. We also thank Biao Zuo and Yuri Veklich at the Electron Microscopy Resources Lab (Perelman School of Medicine, University of Pennsylvania) for assistance with TEM and SEM preparations. Use of confocal microscopes (CDB microscopy core, Perelman School of Medicine, University of Pennsylvania) under the supervision of Dr. Andrea Stout, is greatly appreciated. The contributions of Thadé P.M. Goderie for collection and analysis of human audiometric data. Helger G. IJntema for medical genetic testing of patients, Saskia van der Velde-Visser for EBV transformation and cell culture, and Jailynn Harke for protein co-localization analysis are greatly appreciated. The DOOFNL Consortium consisting of M.F. van Dooren, S.G. Kant, H.H.W. de Gier, E.H. Hoefsloot, M.P. van der Schroeff, L.J.C. Rotteveel, F.G. Ropers, J.C.C. Widdershoven, J.R. Hof, E.K. Vanhoutte, I. Feenstra, H. Kremer, C.P. Lanting, R.J.E. Pennings, H.G. Yntema, R.H. Free and J.S. Klein Wassink-Ruiter, R.J. Stokroos, A.L. Smit, M.J. van den Boogaard, F.A. Ebbens, S.M. Maas, A. Plomp, T.P.M. Goderie, P. Merkus and J. van de Kamp, contributed to the clinical evaluation and medical genetic testing of ~800 unsolved index cases of hearing loss. This work was funded by grants from the National Institutes of Health, R01 DC006254 (D.J.E.), R01 DC014450, R01 DC013774, and R01 DC017741 (J.S.O.), R01 HL133080 (B.L.P.), the Boucai Innovation Fund in Auditory Genomics (D.J.E.), the Center for Engineering MechanoBiology through a grant from the National Science Foundation's Science and Technology Center program: 15-48571 (B.L.P.), and the Heinsius Houbolt Foundation (R.J.E.P., H.K.). A.M.R was supported by the Predoctoral Training Program in Genetics (T32 GM008216) and an NRSA fellowship F31DC014647. A.N. was supported by T32 DC-00011.

AUTHOR CONTRIBUTIONS

T.C., A.M.R., and D.J.E. conceived the study. T.C., A.M.R., S.M.R., and D.J.E. designed and performed mouse molecular, cellular, and genetic studies. M.C., T.C., and B.L.P. performed and analyzed atomic force microscopy (AFM) experiments. A.N. and J.S.O. performed and analyzed VOCTV experiments. K.K.O. performed ABR, DPOAE, and EP recordings. A.M.R. and K.H.K. prepared ESCs for blastocyst injections. J.J.S., J.M.v.d.K., and R.J.E.P performed and supervised the human clinical study. E.K. and C.G. performed bioinformatic analysis of WES data. J.J.S., J.O., and H.K. designed and performed human molecular genetics experiments. T.C., J.S.O., J.J.S., H.K., and D.J.E. wrote the manuscript. All authors analyzed the data, discussed the results, and commented on the manuscript.

DECLARATION OF INTERESTS

The authors declare no competing interests.

INCLUSION AND DIVERSITY

We worked to ensure that the study questionnaires were prepared in an inclusive way. We worked to ensure sex balance in the selection of non-human subjects. One or more of the authors of this paper self-identifies as living with a disability. The author list of this paper includes contributors from the location where the research was conducted who participated in the data collection, design, analysis, and/or interpretation of the work.

Received: November 11, 2020 Revised: February 1, 2021 Accepted: April 16, 2021 Published: May 7, 2021

REFERENCES

Adzhubei, I.A., Schmidt, S., Peshkin, L., Ramensky, V.E., Gerasimova, A., Bork, P., Kondrashov, A.S., and Sunyaev, S.R. (2010). A method and server for predicting damaging missense mutations. Nat. Methods 7, 248–249.

Angelborg, C., and Engström, H. (1972). Supporting elements in the organ of Corti I. Fibrillar structures in the supporting cells of the organ of Corti of mammals. Acta Oto-Laryngologica *73*, 49–60.

Anzai, T., Fukunaga, I., Hatakeyama, K., Fujimoto, A., Kobayashi, K., Nishikawa, A., Aoki, T., Noda, T., Minowa, O., Ikeda, K., and Kamiya, K. (2015). Deformation of the outer hair cells and the accumulation of Caveolin-2 in connexin 26 deficient mice. PLoS One *10*. e0141258.

Arima, T., Uemura, T., and Yamamoto, T. (1986). Cytoskeletal organization in the supporting cell of the guinea pig organ of Corti. Hear. Res. 24, 169–175.

Bekesy, G.v. (1960). Experiments in Hearing (McGraw-Hill).

Bodakuntla, S., Jijumon, A.S., Villablanca, C., Gonzalez-Billault, C., and Janke, C. (2019). Microtubule-associated proteins: structuring the cytoskeleton. Trends Cell Biol 29, 804–819.

Bosman, A.J., and Smoorenburg, G.F. (1995). Intelligibility of Dutch CVC syllables and sentences for listeners with normal hearing and with three types of hearing impairment. Audiology *34*, 260–284.

Brancolini, C., Bottega, S., and Schneider, C. (1992). Gas2, a growth arrest-specific protein, is a component of the microfilament network system. J. Cell Biol. *117*, 1251–1261.

Chan, D.K., and Hudspeth, A.J. (2005). Mechanical responses of the organ of corti to acoustic and electrical stimulation in vitro. Biophys. J. 89, 4382–4395.

Chatzispyrou, I.A., Alders, M., Guerrero-Castillo, S., Zapata Perez, R., Haagmans, M.A., Mouchiroud, L., Koster, J., Ofman, R., Baas, F., Waterham, H.R., et al. (2017). A homozygous missense mutation in ERAL1, encoding a mitochondrial rRNA chaperone, causes Perrault syndrome. Hum. Mol. Genet. *26*, 2541–2550.

Chen, G.D., and Fechter, L.D. (2003). The relationship between noise-induced hearing loss and hair cell loss in rats. Hear. Res. 177, 81–90.

Chen, G.D., Tanaka, C., and Henderson, D. (2008). Relation between outer hair cell loss and hearing loss in rats exposed to styrene. Hear. Res. 243, 28–34.

Collin, R.W., den Hollander, A.I., van der Velde-Visser, S.D., Bennicelli, J., Bennett, J., and Cremers, F.P. (2012). Antisense oligonucleotide (AON)-based therapy for Leber congenital amaurosis caused by a frequent mutation in CEP290. Mol. Ther. Nucleic Acids 1, e14.

Dallos, P., Wu, X., Cheatham, M.A., Gao, J., Zheng, J., Anderson, C.T., Jia, S., Wang, X., Cheng, W.H., SenGupta, S., et al. (2008). Prestin-based outer hair cell motility is necessary for mammalian cochlear amplification. Neuron *58*, 333–339.

Dewey, J.B., Applegate, B.E., and Oghalai, J.S. (2019). Amplification and suppression of traveling waves along the mouse organ of Corti: evidence for spatial variation in the longitudinal coupling of outer hair cell-generated forces. J. Neurosci. 39, 1805–1816.

Dewey, J.B., Xia, A., Müller, U., Belyantseva, I.A., Applegate, B.E., and Oghalai, J.S. (2018). Mammalian auditory hair cell bundle stiffness affects frequency tuning by increasing coupling along the length of the cochlea. Cell Rep 23, 2915–2927.

Dougherty, G.W., Adler, H.J., Rzadzinska, A., Gimona, M., Tomita, Y., Lattig, M.C., Merritt, R.C., Jr., and Kachar, B. (2005). CLAMP, a novel microtubule-associated protein with EB-type calponin homology. Cell Motil. Cytoskeleton *62*, 141–156.

Echarri, A., Pavón, D.M., Sánchez, S., García-García, M., Calvo, E., Huerta-López, C., Velázquez-Carreras, D., Viaris de Lesegno, C., Ariotti, N., Lázaro-Carrillo, A., et al. (2019). An Abl-FBP17 mechanosensing system couples local plasma membrane curvature and stress fiber remodeling during mechanoadaptation. Nat. Commun. 10, 5828.

Fettiplace, R. (2017). Hair cell transduction, tuning, and synaptic transmission in the mammalian cochlea. Compr. Physiol. 7, 1197–1227.

Fisher, J.A., Nin, F., Reichenbach, T., Uthaiah, R.C., and Hudspeth, A.J. (2012). The spatial pattern of cochlear amplification. Neuron *76*, 989–997.

Article



Fridberger, A., Boutet de Monvel, J., and Ulfendahl, M. (2002). Internal shearing within the hearing organ evoked by basilar membrane motion. J. Neurosci. 22, 9850-9857.

Gao, S.S., Wang, R., Raphael, P.D., Moayedi, Y., Groves, A.K., Zuo, J., Applegate, B.E., and Oghalai, J.S. (2014). Vibration of the organ of Corti within the cochlear apex in mice. J. Neurophysiol. 112, 1192-1204.

Geisler, C.D., and Sang, C. (1995). A cochlear model using feed-forward outerhair-cell forces. Hear. Res. 86, 132-146.

Hahn, I., Voelzmann, A., Liew, Y.T., Costa-Gomes, B., and Prokop, A. (2019). The model of local axon homeostasis - explaining the role and regulation of microtubule bundles in axon maintenance and pathology. Neural Dev 14, 11.

Hamernik, R.P., Patterson, J.H., Turrentine, G.A., and Ahroon, W.A. (1989). The quantitative relation between sensory cell loss and hearing thresholds. Hear. Res. 38, 199-211.

Ka, M., and Kim, W.Y. (2016). Microtubule-actin crosslinking factor 1 is required for dendritic arborization and axon outgrowth in the developing brain. Mol. Neurobiol. 53, 6018-6032.

Karavitaki, K.D., and Mountain, D.C. (2007). Evidence for outer hair cell driven oscillatory fluid flow in the tunnel of corti. Biophys. J. 92, 3284-3293.

Katsuno, T., Belyantseva, I.A., Cartagena-Rivera, A.X., Ohta, K., Crump, S.M., Petralia, R.S., Ono, K., Tona, R., Imtiaz, A., Rehman, A., et al. (2019). TRIOBP-5 sculpts stereocilia rootlets and stiffens supporting cells enabling hearing. JCI Insight 4. e128561.

Kemp, D.T. (2002). Otoacoustic emissions, their origin in cochlear function, and use. Br. Med. Bull. 63, 223-241.

Kim, J., Xia, A., Grillet, N., Applegate, B.E., and Oghalai, J.S. (2018). Osmotic stabilization prevents cochlear synaptopathy after blast trauma. Proc. Natl. Acad. Sci. USA 115, E4853-E4860.

Kim, S., Oghalai, J.S., and Applegate, B.E. (2019). Noise and sensitivity in optical coherence tomography based vibrometry. Opt. Express 27, 33333-33350.

Kircher, M., Witten, D.M., Jain, P., O'Roak, B.J., Cooper, G.M., and Shendure, J. (2014). A general framework for estimating the relative pathogenicity of human genetic variants. Nat. Genet. 46, 310-315.

Lee, H.Y., Raphael, P.D., Park, J., Ellerbee, A.K., Applegate, B.E., and Oghalai, J.S. (2015). Noninvasive in vivo imaging reveals differences between tectorial membrane and basilar membrane traveling waves in the mouse cochlea. Proc. Natl. Acad. Sci. USA 112, 3128-3133.

Legan, P.K., Lukashkina, V.A., Goodyear, R.J., Kössl, M., Russell, I.J., and Richardson, G.P. (2000). A targeted deletion in α -tectorin reveals that the tectorial membrane is required for the gain and timing of cochlear feedback. Neuron 28, 273-285.

Liberman, M.C., Gao, J., He, D.Z., Wu, X., Jia, S., and Zuo, J. (2002). Prestin is required for electromotility of the outer hair cell and for the cochlear amplifier. Nature 419, 300-304.

Liu, Y., Gracewski, S.M., and Nam, J.H. (2015). Consequences of locationdependent organ of Corti micro-mechanics. PLoS One 10, e0133284.

Locher, H., de Groot, J.C.M.J., van Iperen, L., Huisman, M.A., Frijns, J.H.M., and Chuva de Sousa Lopes, S.M. (2015). Development of the stria vascularis and potassium regulation in the human fetal cochlea: Insights into hereditary sensorineural hearing loss. Dev. Neurobiol. 75, 1219-1240.

M, M., Van Camp, G., Newton, V., N, G., F, D., and Parving, A. (2003). Recommendations for the description of genetic and audiological data for families with nonsyndromic hereditary hearing impairment. Audiol. Med. 1,

Martin, P., and Swanson, G.J. (1993). Descriptive and experimental analysis of the epithelial remodellings that control semicircular canal formation in the developing mouse inner ear. Dev. Biol. 159, 549-558.

Motallebzadeh, H., Soons, J.A.M., and Puria, S. (2018). Cochlear amplification and tuning depend on the cellular arrangement within the organ of Corti. Proc. Natl. Acad. Sci. USA 115, 5762-5767.

Muroyama, A., and Lechler, T. (2017). Microtubule organization, dynamics and functions in differentiated cells. Development 144, 3012-3021.

Muthu, V., Rohacek, A.M., Yao, Y., Rakowiecki, S.M., Brown, A.S., Zhao, Y.T., Meyers, J., Won, K.J., Ramdas, S., Brown, C.D., et al. (2019). Genomic architecture of Shh-dependent cochlear morphogenesis. Development 146, dev181339.

Nam, J.H., and Fettiplace, R. (2010). Force transmission in the organ of Corti micromachine. Biophys. J. 98, 2813-2821.

Nankali, A., Wang, Y., Strimbu, C.E., Olson, E.S., and Grosh, K. (2020). A role for tectorial membrane mechanics in activating the cochlear amplifier. Sci. Rep. 10, 17620.

Neely, S.T., Johnson, T.A., Kopun, J., Dierking, D.M., and Gorga, M.P. (2009). Distortion-product otoacoustic emission input/output characteristics in normal-hearing and hearing-impaired human ears. J. Acoust. Soc. Am. 126,

Newman, W.G., Friedman, T.B., Conway, G.S., and Demain, L.A.M. (2018). Perrault syndrome. In GeneReviews®, M.P. Adam, H.H. Ardinger, R.A. Pagon, S.E. Wallace, L.J.H. Bean, K. Stephens, and A. Amemiya, eds. (University of Washington), pp. 1993–2021.

Ni, G., Elliott, S.J., and Baumgart, J. (2016). Finite-element model of the active organ of Corti. J. R. Soc. Interface 13, 20150913.

Nilsen, K.E., and Russell, I.J. (2000). The spatial and temporal representation of a tone on the guinea pig basilar membrane. Proc. Natl. Acad. Sci. USA 97. 11751-11758.

Nissim, S., Allard, P., Bandyopadhyay, A., Harfe, B.D., and Tabin, C.J. (2007). Characterization of a novel ectodermal signaling center regulating Tbx2 and Shh in the vertebrate limb. Dev. Biol. 304, 9-21.

Ó Maoiléidigh, D., and Ricci, A.J. (2019). A bundle of mechanisms: inner-ear hair-cell mechanotransduction. Trends Neurosci 42, 221-236.

Oonk, A.M., Beynon, A.J., Peters, T.A., Kunst, H.P., Admiraal, R.J., Kremer, H., Verbist, B., and Pennings, R.J. (2015). Vestibular function and temporal bone imaging in DFNB1. Hear. Res. 327, 227-234.

Oshima, T., Okabe, S., and Hirokawa, N. (1992). Immunocytochemical localization of 205 kDa microtubule-associated protein (205 kDa MAP) in the guinea pig organ of Corti. Brain Res 590, 53-65.

Pfaffl, M.W. (2001). A new mathematical model for relative quantification in real-time RT-PCR. Nucleic Acids Res 29, e45.

Portran, D., Schaedel, L., Xu, Z., Théry, M., and Nachury, M.V. (2017). Tubulin acetylation protects long-lived microtubules against mechanical ageing. Nat. Cell Biol. 19, 391-398.

Pritchard, U. (1878). The development of the organ of Corti. J. Anat. Physiol.

Robison, P., Caporizzo, M.A., Ahmadzadeh, H., Bogush, A.I., Chen, C.Y., Margulies, K.B., Shenoy, V.B., and Prosser, B.L. (2016). Detyrosinated microtubules buckle and bear load in contracting cardiomyocytes. Science 352,

Robles, L., and Ruggero, M.A. (2001). Mechanics of the mammalian cochlea. Physiol. Rev. 81, 1305-1352.

Russell, I.J., Legan, P.K., Lukashkina, V.A., Lukashkin, A.N., Goodyear, R.J., and Richardson, G.P. (2007). Sharpened cochlear tuning in a mouse with a genetically modified tectorial membrane. Nat. Neurosci. 10, 215-223.

Saha, S., and Slepecky, N.B. (2000). Age-related changes in microtubules in the guinea pig organ of Corti. Tubulin isoform shifts with increasing age suggest changes in micromechanical properties of the sensory epithelium. Cell Tissue Res 300, 29-46.

Sanchez-Soriano, N., Travis, M., Dajas-Bailador, F., Gonçalves-Pimentel, C., Whitmarsh, A.J., and Prokop, A. (2009). Mouse ACF7 and Drosophila short stop modulate filopodia formation and microtubule organisation during neuronal growth. J. Cell Sci. 122, 2534-2542.

Sasmal, A., and Grosh, K. (2019). Unified cochlear model for low- and high-frequency mammalian hearing. Proc. Natl. Acad. Sci. USA 116, 13983-13988.

Schwarz, J.M., Cooper, D.N., Schuelke, M., and Seelow, D. (2014). MutationTaster2: mutation prediction for the deep-sequencing age. Nat. Methods 11, 361-362.



Sinha, B., Köster, D., Ruez, R., Gonnord, P., Bastiani, M., Abankwa, D., Stan, R.V., Butler-Browne, G., Vedie, B., Johannes, L., et al. (2011). Cells respond to mechanical stress by rapid disassembly of caveolae. Cell 144, 402-413.

Slepecky, N., and Chamberlain, S.C. (1983). Distribution and polarity of actin in inner ear supporting cells. Hear. Res. 10, 359-370.

Slepecky, N.B. (1996). Structure of the mammalian cochlea. In The Cochlea, P.J. Dallos, A.N. Popper, and R.R. Fay, eds. (Springer-Verlag), pp. 44-129.

Slepecky, N.B., Henderson, C.G., and Saha, S. (1995). Post-translational modifications of tubulin suggest that dynamic microtubules are present in sensory cells and stable microtubules are present in supporting cells of the mammalian cochlea. Hear. Res. 91, 136-147.

Smits, J.J., Oostrik, J., Beynon, A.J., Kant, S.G., de Koning Gans, P.A.M., Rotteveel, L.J.C., Klein Wassink-Ruiter, J.S., Free, R.H., Maas, S.M., van de Kamp, J., et al. (2019). De novo and inherited loss-of-function variants of ATP2B2 are associated with rapidly progressive hearing impairment. Hum. Genet 138 61-72

Soons, J.A., Ricci, A.J., Steele, C.R., and Puria, S. (2015). Cytoarchitecture of the mouse organ of corti from base to apex, determined using in situ twophoton imaging. J. Assoc. Res. Otolaryngol. 16, 47-66.

Stroud, M.J., Nazgiewicz, A., McKenzie, E.A., Wang, Y., Kammerer, R.A., and Ballestrem, C. (2014). GAS2-like proteins mediate communication between microtubules and actin through interactions with end-binding proteins. J. Cell Sci. 127, 2672-2682.

Sugawara, M., Ishida, Y., and Wada, H. (2004). Mechanical properties of sensory and supporting cells in the organ of Corti of the guinea pig cochlea-study by atomic force microscopy. Hear. Res. 192, 57-64.

Szarama, K.B., Gavara, N., Petralia, R.S., Kelley, M.W., and Chadwick, R.S. (2012). Cytoskeletal changes in actin and microtubules underlie the developing surface mechanical properties of sensory and supporting cells in the mouse cochlea. Development 139, 2187-2197.

Testa, G., Schaft, J., van der Hoeven, F., Glaser, S., Anastassiadis, K., Zhang, Y., Hermann, T., Stremmel, W., and Stewart, A.F. (2004). A reliable lacZ expression reporter cassette for multipurpose, knockout-first alleles. Genesis 38, 151-158.

Tolomeo, J.A., and Holley, M.C. (1997). Mechanics of microtubule bundles in pillar cells from the inner ear. Biophys. J. 73, 2241–2247.

Tucker, E.J., Rius, R., Jaillard, S., Bell, K., Lamont, P.J., Travessa, A., Dupont, J., Sampaio, L., Dulon, J., Vuillaumier-Barrot, S., et al. (2020). Genomic sequencing highlights the diverse molecular causes of Perrault syndrome: a peroxisomal disorder (PEX6), metabolic disorders (CLPP, GGPS1), and mtDNA maintenance/translation disorders (LARS2, TFAM). Hum. Genet.

Tucker, J.B., Mogensen, M.M., Paton, C.C., Mackie, J.B., Henderson, C.G., and Leckie, L.M. (1995). Formation of two microtubule-nucleating sites which

perform differently during centrosomal reorganization in a mouse cochlear epithelial cell. J. Cell Sci. 108, 1333-1345.

van de Willige, D., Hummel, J.J., Alkemade, C., Kahn, O.I., Au, F.K., Qi, R.Z., Dogterom, M., Koenderink, G.H., Hoogenraad, C.C., and Akhmanova, A. (2019). Cytolinker Gas2L1 regulates axon morphology through microtubulemodulated actin stabilization. EMBO Rep 20, e47732.

van der Ploeg, C.P., Uilenburg, N.N., Kauffman-de Boer, M.A., Oudesluys-Murphy, A.M., and Verkerk, P.H. (2012). Newborn hearing screening in youth health care in the Netherlands: national results of implementation and follow-up. Int. J. Audiol. 51, 584-590.

Vaser, R., Adusumalli, S., Leng, S.N., Sikic, M., and Ng, P.C. (2016). SIFT missense predictions for genomes. Nat. Protoc. 11, 1-9.

Wall, F.E., Henkel, R.D., Stern, M.P., Jenson, H.B., and Moyer, M.P. (1995). An efficient method for routine Epstein-Barr virus immortalization of human Blymphocytes. In Vitro Cell. Dev. Biol. Anim. 31, 156-159.

Walters, B.J., Yamashita, T., and Zuo, J. (2015). Sox2-CreER mice are useful for fate mapping of mature, but not neonatal, cochlear supporting cells in hair cell regeneration studies. Sci. Rep. 5, 11621.

Wesdorp, M., Murillo-Cuesta, S., Peters, T., Celaya, A.M., Oonk, A., Schraders, M., Oostrik, J., Gomez-Rosas, E., Beynon, A.J., Hartel, B.P., et al. (2018). MPZL2, encoding the epithelial junctional protein myelin protein zero-like 2, is essential for HEARing in man and mouse. Am. J. Hum. Genet.

Xu, Z., Schaedel, L., Portran, D., Aguilar, A., Gaillard, J., Marinkovich, M.P., Théry, M., and Nachury, M.V. (2017). Microtubules acquire resistance from mechanical breakage through intralumenal acetylation. Science 356, 328-332.

Yoon, Y.J., Steele, C.R., and Puria, S. (2011). Feed-forward and feed-backward amplification model from cochlear cytoarchitecture: an interspecies comparison. Biophys. J. 100, 1-10.

York, J.P., Ren, Y.A., Zeng, J., Zhang, B., Wang, F., Chen, R., Liu, J., Xia, X., and Zhang, P. (2016). Growth arrest specific 2 (GAS2) is a critical mediator of germ cell cyst breakdown and folliculogenes is in mice. Sci. Rep. 6, 34956.

Yu, W.M., and Goodrich, L.V. (2014). Morphological and physiological development of auditory synapses. Hear. Res. 311, 3-16.

Zetes, D.E., Tolomeo, J.A., and Holley, M.C. (2012). Structure and mechanics of supporting cells in the guinea pig organ of Corti. PLoS One 7, e49338.

Zhang, T., Dayanandan, B., Rouiller, I., Lawrence, E.J., and Mandato, C.A. (2011). Growth-arrest-specific protein 2 inhibits cell division in Xenopus embryos. PLoS One 6, e24698.

Zheng, J., Furness, D., Duan, C., Miller, K.K., Edge, R.M., Chen, J., Homma, K., Hackney, C.M., Dallos, P., and Cheatham, M.A. (2013). Marshalin, a microtubule minus-end binding protein, regulates cytoskeletal structure in the organ of Corti. Biol. Open 2, 1192-1202.

Developmental Cell Article



STAR***METHODS**

KEY RESOURCES TABLE

REAGENT or RESOURCE	SOURCE	IDENTIFIER
Antibodies (dilution)		
Mouse monoclonal anti-GAS2(F12) (1:400)	Santa Cruz	Cat#sc-398669; RRID: AB_2884899
Rabbit anti-GAS2 (1:1000)	Abcam	Cat#b109762; RRID: AB_10864608
Rabbit anti-MYO7A (1:350)	Proteus Biosc.	Cat#25-6790; RRID: AB_10015251
Rabbit anti Detyrosinated alpha- tubulin (1:200)	Abcam	Cat#ab48389; RRID: AB_869990
Mouse anti-Alpha-tubulin (1:400)	Cell Signaling	3873; RRID: AB_1904178
Mouse anti-Acetylated-tubulin (1:400)	Sigma	Cat#T6793; RRID: AB_477585
Rabbit anti-SOX2 (1:200)	Chemicon	Cat#AB5603; RRID: AB_2286686
Mouse anti-Neurofilament (1:400)	DSHB	Cat#2H3; RRID: AB_531793
Goat anti-KCNQ1 (1:300)	Santa Cruz	Cat#sc-10646; RRID: AB_2131554
Mouse anti-ATP1A1 (1:250)	DSHB	Cat#A5
Rat anti-CD44 (1:200)	BD Pharmingen	Cat#553131; RRID: AB_394646
Rabbit anti-Claudin-11 (1:100)	Thermo Fisher	Cat#36-4500; RRID: AB_2533259
Mouse anti-Connexin-26/GJB2 (1:200)	Thermo Fisher	Cat#71-0500; RRID: AB 2533971
Mouse anti-CAV2 (1:800)	BD Biosciences	Cat#610684
Mouse anti-Prestin (1:200)	Santa Cruz	Cat#sc-293212
Mouse anti-GAPDH (1:1000)	Invitrogen	Cat# MA5-15738; RRID: AB_10977387
Rabbit anti-goat IGG Alexa488 (1:400)	Molecular probes	Cat#A-11078; RRID: AB_141838
· ,	•	· –
Donkey anti-rat Alexa488 (1:400)	Molecular probes	Cat#A-21208; RRID: AB_141709
Goat anti-mouse Alexa488 (1:400)	Thermo Fisher	Cat#A28175; RRID: AB_2536161
Goat anti-rabbit Alexa594 (1:400)	Thermo Fisher	Cat#A-11037; RRID: AB_2534095
RDye® 680LT Goat anti-Mouse gG (1:20000)	LI-COR	925-68020; RRID: AB_2687826
RDye® 800CW Goat anti-Rabbit lgG (1:20000)	LI-COR	925-32211; RRID: AB_2651127
Chemicals, peptides, and recombinant protein	s	
Phalloidin conjugated Alexa488 (1:400)	Molecular Probes	A12379
Odyssey® Blocking Buffer	LI-COR	927-40000
Tamoxifen	Sigma	T5648
Hoechst (1:1000)	Thermo Fisher	62249
Paraformaldehyde	Electron Microscopy Sciences	15710
Thiocarbohydrazide	Electron Microscopy Sciences	21900
Osmium tetroxide, 2% Aqueous Solution	Electron Microscopy Sciences	19152
Glutaraldehyde, 5% in 0.1M Phosphate Buffer, pH 7.4	Electron Microscopy Sciences	16539-30
Phosphate Buffer, 0.1M	Electron Microscopy Sciences	19340-72
Sodium Cacodylate Buffer	Electron Microscopy Sciences	11650
Methyl Salicylate	Sigma	M2047
Critical commercial assays		
SiR-tubulin kit (1:1000)	Cytoskeleton, Inc	Cat#CY-SC002
GoTag gPCR Master Mix	Promega	A6002
SuperScript™ IV Reverse Transcriptase	Thermo Fisher	18090010
Experimental models: cell lines		1000010
Mouse: Gas2tm1a(EUCOMM)Hmgu	https://www.eummcr.org	HEPD0681_7_F03

(Continued on next page)



Continued		
REAGENT or RESOURCE	SOURCE	IDENTIFIER
Experimental models: organisms/strains		
Mouse: Gas2tm1a/+	This paper	N/A
Mouse: B6.129S4-Gt(ROSA) 26Sortm2(FLP*)Sor/J	The Jackson Labs	012930
Mouse: Gas2tm1c/tm1c	This paper	N/A
Mouse: Sox2creER	The Jackson Labs	017593
Oligonucleotides		
Primers for qPCR of GAS2 cDNA, see Table S1	This paper	N/A
Genotyping primers for Gas2 alleles, see Table S3	This paper	N/A
Software and algorithms		
ImageJ	NIH	https://imagej.nih.gov/ij/
Prism 8	GraphPad	N/A
Origin 2019	Origin Lab	https://www.originlab.com/2019
Matlab 2019	Matwork (https://www.mathworks.com/)	623588
QuantStudio Design & Analysis Software 1.4.3	Thermo Fisher	N/A
Alamut Visual 2.13	Interactive Biosoftware	N/A
Other		
Leica TCS SP8 MP system	Leica	https://www.leica-microsystems.com/ products/confocal-microscopes/p/leica- tcs-sp8-mp/downloads/
FEI Quanta 250 SEM	FEI	http://www.biotech.iastate.edu/wp_single/wp-content/uploads/2012/01/quanta.pdf
Jeol-1010 transmission electron microscope TEM	JEOL	https://iubemcenter.indiana.edu/ equipment/microscopes/jeol-jem- 1010/index.html
Zeiss LSM 880 with Fast Airyscan module	Zeiss	https://www.zeiss.com/microscopy/us/ dynamic-content/news/2014/news-lsm- 880.html
Chiaro Nanoindenter	Optics 11 Life	https://www.optics11life.com/products/ chiaro-nanoindenter/
Echo Revolve Microscope	Echo	https://discover-echo.com/revolve

RESOURCE AVAILABILITY

Lead contact

Further information and requests for resources and reagents should be directed to and will be fulfilled by the Lead Contact, Douglas J. Epstein, Ph.D. (epsteind@pennmedicine.upenn.edu).

Materials availability

Gas2 mutant mice generated in this study will be made available on request, but we may require a payment and/or a completed Materials Transfer Agreement if there is potential for commercial application.

Data and code availability

This study did not generate any unique datasets or code.

EXPERIMENTAL MODEL AND SUBJECT DETAILS

Mouse lines

All mouse experiments were performed in accordance with the ethical guidelines of the National Institutes of Health and with the approval of the Institutional Animal Care and Use Committee of the University of Pennsylvania. Mice were housed in Thoren caging

Article



units under a constant 12-hour light/dark cycle. The Gas2^{tm1a/+} mouse line was generated from ES-cells obtained from the European Conditional Mouse Mutagenesis Program (Clone: HEPD0681_7_F03) (Figure S2A). ES-Cells were injected into albino C57B/6N-tac blastocysts at the Transgenic and Chimeric Mouse Facility (Perelman School of Medicine, University of Pennsylvania). High percentage chimeras (>90% black/agouti coat) were bred to albino C57B/6N-tac mice and the resulting pups were screened for the Gas2^{tm1a} allele by coat color and PCR genotyping. Primers flanking the floxed Gas2 exon 5 (F-TTGGATCATATGGAGAGAGCCAT, R-GGGCAT ATCACAGGCCCATA) amplified a 223 bp product from the wild type allele and a 257 bp product from the Gas2^{tm1a} allele using the following PCR conditions: 95°C for 5 min, 95°C for 30 sec, 58°C for 30 sec, 72°C for 18 sec, steps 2-4 repeated for 31 cycles, 72°C for 10 min. Gas2^{tm1a/+} mice were maintained on a C57B/6N-tac background for at least 10 generations. To generate mice with a floxed allele of Gas2 (Gas2^{tm1c}), Gas2^{tm1a/+} mice were crossed to the FLPo deletor strain (B6 ROSA26Flpo, The Jackson Laboratory) to remove the lacZ-Neomycin cassette (Figure S2B). Gas2tm1c/+ mice were intercrossed after segregating away the FLPo transgene and maintained as homozygotes. To generate conditional knockout mice lacking GAS2 in supporting cells (cGas2), Gas2^{tm1c/tm1c} mice were crossed to the Sox2^{CreER/+} line (B6; 129S- Sox2^{tm1)cre/ERT2)Hoch/J, The Jackson Laboratory) (Figure S2C). Sox2^{CreER/+};} Gas2^{tm1c/+} mice were then crossed to Gas2^{tm1c/tm1c} mice to generate Sox2^{CreER/+}; Gas2^{tm1c/tm1c} (cGas2) and control (Sox2^{CreER/+}; Gas2^{tm1c/+}) pups that were administered tamoxifen (4mg/30g body weight) once a day for two consecutive days starting at P1 to induce Gas2 recombination (Figure S6). Genotyping primers for Gas2 mutants are listed in Table S3. Male and female mice were used in all experiments with no obvious differences in auditory phenotypes between the sexes.

Human subjects

The study of human subjects was approved by the medical ethics committee of the Radboudumc (registration number: NL33648.091.10) and performed in accordance with the principles of the Declaration of Helsinki. Written informed consent was obtained from all participants or their legal representatives. Approximately 800 index cases with audiometrically defined hearing loss were screened for mutations by WES which did not reveal positive findings on genes known to be associated with hereditary hearing loss. Results were compared to unaffected family members if available, the gnomAD database (v.2.1.1) and the WES dataset (>15,000 exomes) at Radboud University Medical Center.

METHOD DETAILS

In situ hybridization

Embryos were collected from timed pregnant females (vaginal plug = E0.5). Heads were dissected at the level of the posterior hindbrain and fixed for 2 hours in 4% paraformaldehyde at 4°C, then washed in PBS. Samples were cryoprotected overnight in 30% sucrose/PBS then snap frozen in OCT embedding compound (Sakura Finetek Torrence, CA). Samples were serially sectioned along the transverse plane. Sections were hybridized with digoxigenin- UTP-labeled riboprobes as previously described (Nissim et al., 2007).

Inner ear paint fill

Paint fills were performed essentially as described (Martin and Swanson, 1993) with the use of White-Out Plus (Bic, Milford, CT, USA) as the contrast medium. Briefly, embryos were dissected at E14.5 in PBS at 4°C. The heads were bisected along the midline, brains removed, and fixed overnight in Bodian fixative. The heads were rinsed in 100% EtOH and stored overnight at room temperature. The heads were placed in methyl salicylate until transparent. Glass needles were filled with White-Out plus diluted in methyl salicylate to 0.25% and injected into the utricle, visualized under a dissecting microscope, until the inner ear became opaque.

Whole mount cochlear preparations

Inner ears were dissected and fixed in 4% paraformaldehyde for 2 hours or overnight at 4°C, then washed in PBS. The inner ears were decalcified in 0.25M EDTA for several hours (P14), for 1 day (P25), for 2 days (P42) or for 3 days (P60) until the bone was completely soft. Cochleae were then microdissected in 0.1% PBST to expose the sensory epithelium, and incubated with antibodies found in the key resources table.

Immunohistochemistry

Inner ears were processed for immunohistochemistry in the same fashion as for in situ hybridization. Inner ear sections were stained with DAPI and antibodies found in the key resources table. Specimens were imaged on a Leica TCS SP8 MP system using 63 x oil or 20× objectives. Stacks of confocal images were acquired with a Z step of 0.37 μm and processed using ImageJ software. Specimens in Figures 1L-1N were imaged on a Zeiss LSM 880 confocal microscope with Airyscan using 63x/1.4 oil objectives and acquired using ZEN v2.3 software.

Western blot

The organ of Corti was isolated from two Gas2^{tm1a/tm1a} and control mice at P0 in RIPA buffer and protein extraction was performed by manual homogenization. Protein concentration was measured using a Bradford assay. Protein lysates were prepared for gel electrophoresis by adding 4X Laemmli Sample Buffer (BIO-RAD, 1610747) to a final concentration. Samples were heat-denatured at 100 °C for 5 min, and 30 µg of total protein was loaded into each well of a 4-15% mini-protein TGX gel (BIO-RAD 10-well, 1.5 mm; Cat. #456-1084). Protein gels were run for 30 min at 80V then 90 min at 110V at room temperature on a BIO-RAD mini-protein



Developmental CellArticle

Tetra electrophoresis system (10025025) using BioRad Power Supply (Power/PAC 300), then transferred onto a PVDF membrane (0.2 μ m, 7*8.5cm size; Cat. #16201745) for 10 min at 250mA then 60 min at 280mA with ice cold water. The membrane was blocked with Intercept (PBS) Blocking Buffers (P/N: 927-70001) for 1 hour at room temperature. Primary antibodies: anti-N-terminal GAS2 (ab109762; 1:500), and anti-GAPDH (Invitrogen, MA5-15738; 1:1000). Secondary antibodies (Licor) used: goat anti-rabbit IRDye 680RD, and goat anti-mouse IRDye 800CD at dilutions of 1:10,000 and incubated for 1 h at room temperature. Standard protocols were used for the Odyssey Infrared Imaging System (LI-COR) for visualization and quantification.

Auditory Brainstem Response

All recordings were from the left ear. ABR recording was carried out using Tucker-Davis Technologies (TDT) System II hardware and software. Animals were anesthetized using ketamine and xylazine (80/15 mg/kg, intraperitoneal injection) and positioned dorsally in a custom head holder. Subdermal platinum needle electrodes (Grass) were placed in the mid-back (ground), behind the right pinna (reference), and at the vertex (active). Body temperature was monitored throughout testing using a rectal probe, and maintained at 37.5 ± 1.0°C using a DC current-based isothermal pad (FHC). A TDT ES-1 speaker was placed 7 cm along the interaural axis. Stimuli were 5 ms tone bursts (1000 repetitions, 20/s, 1.0 ms rise/fall time) at frequencies of 5, 10, 20, 28.3, 40 and 56.6 kHz. Responses were amplified x100,000 and filtered at 100-10,000 Hz. Thresholds were taken to be the lowest sound level for which Wave I could be identified, using a 5dB minimum step size.

Distortion product otoacoustic emissions

DPOAE (2f1-f2) recordings were obtained in a separate session from ABR recordings, but the animals were prepared similarly as for ABRs. DPOAE iso-input (DP-gram) responses were obtained using EMAV (S. Neely, Z. Liu, BTNRH) in conjunction with TDT and custom hardware using f2 frequencies ranging from 5-40 kHz. F1 frequencies were given by f2/1.2. L1 and L2 levels were set at 75 and 65 dB SPL, respectively. Stimuli were delivered to the ear using a custom coupler inserted using an operating scope. Each channel was output to a TDT EC-1 speaker. DPOAE responses were recorded using a Knowles FC-23652-P16 microphone calibrated to 40 kHz.

Endocochlear potential recording

After ABR and DPOAE recording, animals underwent a single terminal EP measurement from the cochlear lower basal turn of the left ear. Animals were anesthetized (60 mg/kg sodium pentobarbital, IP) and positioned ventrally in a custom head holder. Core temperature was maintained at 37.5 ± 1.0 °C using a thermostatically-controlled heating pad in conjunction with a rectal probe (Yellow Springs Instruments Model 73A). An incision was made along the midline of the neck and soft tissues were blunt dissected and displaced laterally to expose the trachea and left bulla. A tracheostomy was then made and the musculature over the bulla was cut posteriorly to expose the bone overlying the round window. Using a fine drill, a hole was made in the left cochlear capsule directly over scala media of the lower basal turn. Glass capillary pipettes (40-80 M Ω) filled with 0.15 M KCl were mounted on a hydraulic microdrive (Frederick Haer) and advanced until a stable positive potential was observed that did not change with increased electrode depth. The signal from the recording electrode was led to an AM Systems Model 1600 intracellular amplifier. A silver/silver chloride ball inserted into the neck muscles served as ground.

Scanning electron microscopy (SEM)

Gas2 mutant and control cochleae were harvested at P25 and fixed in 2.5% glutaraldehyde in 0.1 M cacodylate buffer for 2 hours at room temperature. The inner ears were decalcified in 0.25M EDTA for three days at 4°C. After decalcification, the inner ears were post-fixed in 1% OsO4 for 60 minutes (2x). The sensory epithelia were then dissected in distilled water. Specimens were dehydrated in a graded ethanol series, dried at the critical point in liquid CO₂, sputter coated with platinum (5.0 nm, controlled by a film-thickness monitor), and imaged with a field-emission SEM (FEI Quanta 250).

Transmission electron microscopy (TEM)

Inner ears were dissected from postnatal animals after euthanasia with CO_2 . The apical turn was opened by cutting a hole in the otic capsule and the cochlea was perfused through the round window every 15 minutes with a mixture of 2% glutaraldehyde and 1% tannic acid in PBS for 90 minutes. The inner ear was then decalcified in 0.25M EDTA overnight at 4°C. The otic capsule, spiral ganglia and stria vascularis were removed to expose the sensory epithelium, which was postfixed in 1% OsO_4 for 90 minutes. The samples were submitted to the Electron Microscopy Resources Lab (Perelman School of Medicine, University of Pennsylvania), dehydrated in ethanol, permeated in propylene oxide, and embedded in Epon resin. Sections were taken on a diamond wafer blade, stained with uranyl acetate and lead citrate and imaged on Jeol-1010 transmission electron microscope.

Cochlear explant culture

Mice were decapitated on P9, and the organs of Corti were dissected in Leibovitz's L-15 medium. The tissues were adhered to petri dishes coated with BD CellTak (BD Life Sciences) and filled with Dulbecco's modified eagle's medium (DMEM)/F12 (1:1), containing 97% DMEM, 1% fetal bovine serum (FBS), 1% N-2, and 1% ampicillin. Cultures were maintained at 37 °C in an atmosphere containing 5% CO₂ for 1 to 5 days. Microtubule (SiR-tubulin) and DNA (Hoechst) stains were added to cultures 60 minutes and 10 minutes, respectively, prior to AFM measurements and washed out before the start of each experiment.





Atomic Force Microscopy (AFM)

An Echo Revolve Microscope equipped with a standard fluorescence package and Olympus 4x, 10x, 20x and 40x APO objectives was mounted on a passively isolated optical table. A Chiaro Nanoindenter (Optics 11 Life) was affixed to the optical table via the provided pedestal and positioned such that the end of the AFM cantilever was centered in the microscope field of view. A single AFM probe was cleaned with deionized water and 70% EtOH and reused for each experiment to reduce potential probe-probe variability. The optical interference pattern of the probe and a calibration via an indentation on an uncoated glass substrate prior to each experiment was used as a confirmation of probe accuracy and integrity on each experimental day. The indenter was a sphere of 9 µm radius affixed to a cantilever and 0.05 N/m purchased from Optics 11 Life. The laptop, controller and interferometer hardware were operated from a table adjacent to the optical table. Autofluorescence of the bead in the Texas Red channel and SiR tubulin labelling (Cy5 channel) of the pillar and Deiters' cells was used to accurately position the AFM probe over the respective cells. Repeated measurements with 2 µm excursions for a total of 60 µm were used to determine the stiffness of each cell type for each cochlea. The AFM cantilever was positioned over the cochlea such that a total piezo travel distance of 15 µm at a speed of 10 μm/s was sufficient to obtain 2-6 μm of indentation into the cells and the stiffness was determined by fitting the first 50% of the indentation curve to the Hertz equation for a spherical indenter, which assumes that the organ of Corti is a homogenous linearly elastic isotropic incompressible material, as previously applied (Szarama et al., 2012; Katsuno et al., 2019). Fitting was conducted by the Piuma Software (Optics 11 Life).

Representative indentation curves are shown in Figure S8. The slope of the indentation curve was fitted to the Hertz equation:

$$F(\delta) = \frac{4}{3} \frac{E}{(1 - v^2)} R^{1/2} \delta^{3/2}.$$

Where F is the force, E is the Young's Modulus, R is the radius of the indenter, and δ is the depth of indentation.

Cochlear vibration measurements

Volumetric optical coherence tomography and vibrometry (VOCTV) was used to image and measure vibrations from the intact mouse cochlea, as described in (Lee et al., 2015). Mice (P42-P47) of either sex were anesthetized with ketamine (80-100 mg/kg) and xylazine (5-10 mg/kg), placed on a heating pad, and the skull was fixed to a custom head holder with dental cement. A ventrolateral surgical approach was then used to access the left middle ear bulla, which was widely opened so that the otic capsule bone and middle ear ossicles could be visualized. To obtain cross-sectional images of the apical cochlear turn, the source beam was scanned across the otic capsule bone. Sound-evoked vibrations were then measured from one point on the basilar membrane with 100 ms pure-tones presented via a speaker (Fostex FT17H) positioned close to the eardrum. Displacement magnitudes and phases were obtained with stimulus frequencies ranging from 1-15 kHz in 0.5 kHz steps and stimulus levels from 10-80 dB SPL in 10 dB steps. After sacrificing the mouse via anesthetic overdose, the vibration measurements were repeated to collect post-mortem data. All displacement responses included in this report were required to have magnitudes falling at least three standard deviations above the mean of the measurement noise floor at surrounding frequencies (Kim et al., 2019). Significant differences between Gas2 mutant and control mice were assessed using the non-paired, two-tailed t-test in MATLAB.

DNA sequencing and variant identification

DNA was extracted from peripheral blood samples according to standard procedures. For subjects V.2, V.5, and V.6 exomes were enriched with the Agilent SureSelect Human All Exon V5 kit (Agilent, Santa Clara, CA, USA) and whole-exome sequencing (WES) was performed on an Illumina HiSeq2000 or 4000 sequencer by BGI Europe (Copenhagen, Denmark). Read alignment, variant calling, variant annotation, and CNV analysis were performed as described (Smits et al., 2019). Mean 20x coverage of the enriched regions in WES ranged between 95.5 – 97.1%. Initially, 173 genes associated with hearing loss were evaluated in a medical genetics setting, both on shared and individual level (gene list version DG-2.17; Hereditary Hearing Loss Exome Panel Genome Diagnostics Nijmegen-Maastricht (https://order.radboudumc.nl/en/genetics). Subsequently, the complete exome was evaluated by selecting variants shared by all three subjects, according to the criteria described below. Segregation analysis of selected variants was carried out by Sanger sequencing, as described (Wesdorp et al., 2018). Primer sequences are provided in Table S1.

GAS2 mutations and family data

Candidate variants compliant with recessive inheritance were selected as follows: ≥2 variants in a gene, allele frequency ≤1% in gnomAD (version 2.1.1), both in combined and African/African American exome datasets, and our in-house WES database (~15,000 alleles) and ≥5 variant reads, located in exonic regions and (canonical) splice sites. For homozygous variants, per cent variant reads had to be ≥ 80 and for (potentially) compound heterozygous variants ≥ 20 and ≤ 90 . Synonymous variants were evaluated when present in homozygous state or in canonical splice sites.

Prediction of a potential deleterious effect of missense variants was performed with CADD PHRED (≥15)(Kircher et al., 2014), SIFT (≤0.05)(Vaser et al., 2016), PolyPhen-2 (PPH2, ≥0.450)(Adzhubei et al., 2010) and Mutation Taster (deleterious)(Schwarz et al., 2014). Values for predicted deleteriousness are indicated between brackets. Segregation analysis was performed if at least two of the tools predicted a deleterious effect for a homozygous variant or for ≥2 potentially compound heterozygous variants in a certain gene. A potential effect on splicing was predicted using the four algorithms (SpliceSiteFinder, MaxEntScan, NNSPLICE, GeneSplicer)



available in Alamut Visual (version 2.13, Interactive Biosoftware, Rouen, France). A change of ≥5% of splice site scores in at least two of the tools was regarded as significant. Also, PPH2 and SIFT scores were determined via Alamut Visual.

Clinical evaluation

Medical history was taken from all study participants and special attention was paid to non-genetic causes of hearing loss (e.g. perinatal issues or ototoxic medication). The age of onset of hearing loss was congenital when identified at newborn hearing screening or determined by the age at diagnosis (van der Ploeg et al., 2012). Affected subjects underwent general ear, nose and throat examination and were evaluated for the presence of dysmorphic features by a clinical geneticist. Both affected and unaffected individuals underwent audiometric testing. Pure tone (conditioned play for subject V.7) audiometry, speech audiometry and click-evoked automated brainstem response measurements were performed in a sound-attenuating booth, according to current standards (International Organization for Standardization; ISO 8253-1:2010, ISO 389-1, ISO 389-5 and ISO 389-6) (Smits et al., 2019; Bosman and Smoorenburg, 1995). Individuals were considered affected when pure tone thresholds for at least three frequencies were above the frequency-specific 95th percentile of age- and sex-specific thresholds (ISO 7029:2017) for the best hearing ear. The lowest age for which this standard can be applied is 18 years. Audiometric data were described according to the GENDEAF guidelines (M et al., 2003). Measurements of transient evoked otoacoustic emissions (TEOAEs) and distortion product (DPOAEs) were performed according to current standards. DPOAE input/output (I/O) functions were measured as described (Neely et al., 2009). Vestibular function was assessed by electronystagmography, calorisation, rotary chair stimulation and video head impulse tests in subjects V.2 and V.5, as described previously (Oonk et al., 2015). Subjects V.6 and V.7 underwent video head impulse tests. Unaffected siblings also underwent a video head impulse test, as controls. Subject IV.1 did not participate in clinical evaluations and subject V.1 did not consent for the study.

RT-PCR

Aberrant splicing resulting from the GAS2 c.723+1G>A variant was experimentally addressed by RT-PCR. For this, B-lymphoblast cells of subjects IV.1, IV.2, and V3-V5 were immortalized by transformation with the Eppstein-Barr virus (EBV), as described (Collin et al., 2012; Wall et al., 1995). Total RNA was isolated from EBV-transformed cells with use of the NucleoSpin RNA II isolation kit (Machery Nagel, Düren, Germany). Treatment of cells with cycloheximide (CHX, cat. no. C4859, Sigma Aldrich) was performed at a final concentration of 1 μl/mL for 4 hours at 37°C. For cDNA synthesis with the SuperScript IV cDNA synthesis kit (Thermo Fisher Waltham, MA, USA), 1 µg RNA was used. RT-PCR was performed with primer combinations listed in Table S1, and followed by visualization using agarose gel electrophoresis. GAPDH (NM_002046.5) was used as cDNA input control. Sanger sequencing of amplicons was performed.

QPCR

Quantitative PCR (qPCR) was performed with primers designed to detect retention of intron 6 sequences and, for comparison, primers for GAS2 exons 3-4 and for GUSB exons 2-3 (NM_000181) as reference gene (Table S1). Primer sets were validated using a dilution series of 4x, 8x, 16x, 32x and 64x of cDNA of individual V.5. The slopes of primer validation plots were between 0.99 and 1.04 with R² values > 0.99. Reaction mixtures were prepared with the GoTaq qPCR Master Mix (Promega, Madison, WI, USA) according to the manufacturer's protocol. Amplifications were performed with the QuantStudio 3 System (Thermo Fisher). Three independent experiments were performed with qPCR reactions in triplicate. Experimental design and data analysis was performed using the QuantStudio Design & Analysis Software 1.4.3. Relative gene expression levels, as compared to GUSB, were determined with the ΔCt method (Pfaffl, 2001). A one-way ANOVA followed by a least significant difference t-test was employed to identify potentially significant differences.

QUANTIFICATION AND STATISTICAL ANALYSIS

Statistical analysis was performed using GraphPad Prism 8 software (Graphpad Software Inc., San Diego, CA, USA). Normality was assessed using Shapiro-Wilk and Kolmogorov-Smirnov tests. Relevant information for each experiment including sample size, statistical tests and p-values are described in the figure legends. In all cases P<0.05 is considered statistically significant.

Quantification of pillar cell length and distance between hair cells was performed on phalloidin and α-tubulin stained transverse sections and whole mount images using ImageJ. At least two pillar cells were measured per sample from a minimum of three samples taken from the mid-basal turn of the cochlea.

Quantification of detyrosinated α-tubulin fluorescence was performed on binary thresholded images and total white (positive) pixels per unit area was calculated using ImageJ. Six inner and outer pillar cells were measured per sample from a minimum of three samples taken from the mid-basal turn of the cochlea.

Tortuosity measurements were calculated by dividing the actual length of the Deiters' cell phalangeal process by the shortest distance from beginning to end using ImageJ on scanning electron microscope images.

Microtubule density was calculated by dividing the total number of microtubules on a given section by the total area of the section (µm²) from transmission electron microscopy images using ImageJ. Measurements were performed on 3 cells per sample from a minimum of 3 samples taken from the mid-basal turn of the cochlea.





Quantification of the area of organized microtubules in pillar and Deiters cell was performed on transmission electron microscopy images using ImageJ. Microtubules were considered organized If one microtubule was surrounded by eight other equidistant microtubules. Measurements were performed on 3 cells per sample from a minimum of 3 samples taken from the mid-basal turn of the

Co-localization of GAS2 and dTyr α -tubulin was performed using Imaris 9.3.1 software. The Coloc package was utilized with thresholding and applied uniformly across all images. The data in Figure 10 are presented as the percent volume B above threshold colocalized, where B is the volume of dTyr α-tubulin. All experiments were replicated in cochleae from at least three independent animals.